Mon. Not. R. Astron. Soc. **272,** 369–388 (1995)

The rich O II recombination spectrum of the planetary nebula NGC 7009: new observations and atomic data

X.-W. Liu,[1,3] P. J. Storey,[1] M. J. Barlow[1] and R. E. S. Clegg[2]
[1] *Department of Physics and Astronomy, University College London, Gower Street, London WC1E 6BT*
[2] *Royal Greenwich Observatory, Madingley Road, Cambridge CB3 0EZ*
[3] *Beijing Astronomical Observatory, Chinese Academy of Sciences, Beijing 100080, P.R. China*

Accepted 1994 August 22. Received 1994 July 27; in original form 1994 March 21

ABSTRACT

We present new spectrophotometric observations of the rich O II optical recombination line spectrum of the planetary nebula NGC 7009, obtained at a spectral resolution of about 1 Å (FWHM). New intermediate coupling quantal calculations of O II radiative recombination coefficients for the 3d–3p and 4f–3d transitions are presented. The effect of departure from pure LS-coupling is shown to be important. Excellent agreement is found between the observed relative intensities of the O II lines and those calculated from recombination theory allowing for intermediate coupling effects. C, N and O abundances based on our recombination line measurements are derived. In all cases, they are about a factor of 5 higher than the corresponding values deduced from collisionally excited lines, indicating that the discrepancy between the abundances derived from these two different types of emission lines, previously known to exist for C^{2+}, is a common phenomenon, and is probably caused by the same physical process. The nature of this process is still not known. If the discrepancy is due to temperature fluctuations, the implied rms temperature fluctuation parameter t^2 is about a factor of 2 larger than that derived by comparing the temperatures deduced from the [O III] forbidden line ratio and from the ratio of the nebular continuum Balmer discontinuity to Hβ. However, if we adopted the electron temperature derived from nebular continuum Balmer discontinuity instead of that from the [O III] forbidden line ratio, the C and N abundances deduced from ultraviolet collisionally excited lines would come into agreement with those deduced from the optical recombination lines, although the abundance of oxygen deduced from the optical forbidden lines would still be a factor of 2 lower than the corresponding value obtained from the optical recombination lines. The O/H abundance ratio derived from our recombination line analysis of NGC 7009 is more than a factor of 2 higher than the solar oxygen abundance.

Key words: atomic data – atomic processes – ISM: abundances – planetary nebulae: individual: NGC 7009.

1 INTRODUCTION

Studies of optical recombination lines from heavy elements are of great interest, because they are valuable abundance indicators. Abundances derived from them have the advantage that they are almost independent of the temperature structure of the objects under study. On the other hand, heavy-element abundances derived using the classic method based on forbidden line measurements are sensitive to the electron temperature and will tend to underestimate the actual heavy-element abundances if small temperature inhomogeneities are present (Peimbert 1967; Liu & Danziger 1993b). In addition, optical recombination lines can be used for objects located in highly obscured regions like the Galactic Bulge where no UV data are obtainable.

An early systematic study of optically permitted lines in gaseous nebulae was presented by Grandi (1976), who tried to identify the dominant excitation mechanism for individual lines by constructing photoionization models. He showed that some combination of recombination, resonance fluorescence by starlight, and resonance fluorescence by other nebular emission lines could successfully account for the

observed strengths of most of the lines. In particular, he found that radiative recombination dominated the excitation of the rich O II optical permitted lines detected in the Orion nebula. French (1983) obtained carbon abundances in six planetary nebulae (PNe) from optical recombination lines of C II, C III and C IV, without resort to UV observations. Clegg et al. (1987) made use of N IV λ4606 and O IV λ4632 to derive the abundances of N^{4+} and O^{4+}, respectively, in NGC 3918. Barlow & Storey (1993) reported observations of dielectronic and radiative recombination lines from C II and O II from the stellar wind of WC10 central star CPD − 56°8032, and derived the wind temperature and C/He and O/He ratios.

A serious long-standing problem in nebular abundance studies is that the C^{2+} abundances derived from the C II recombination line $4f\,^2F°–3d\,^2D$ λ4267, the best-studied line of this type, are generally (but not always) higher than those deduced from the collisionally excited λ1908 line of C III, by factors of 3–10 in some cases (e.g. Kaler 1986; Barker 1991, and references therein). Various explanations for this discrepancy have been proposed, yet no consensus has been reached; the discrepancy has remained as the observing techniques have improved (Clegg 1987a). One difficulty in interpreting the C II λ4267 line is that it has usually been the only recombination line observed from C II. In the only case where other lines like $3d\,^2D–3p\,^2P°$ λ7236 and $3p\,^2P°3s\,^2S$ λ6578 have been detected (Monk, Barlow & Clegg 1990), their intensities relative to λ4267 were only in fair agreement with theoretical predictions. Studies of recombination lines from other ions could shed light on this problem.

The planetary nebula NGC 7009 has been well known for its unusually rich and strong O II optical permitted lines ever since the early high-resolution photographic spectroscopy observations of Aller & Kaler (1964; see also Kaler & Aller 1969), who identified more than 100 O II permitted transitions in its optical spectrum. These lines are almost certainly excited by recombination, since other possible excitation mechanisms such as dielectronic recombination, radiative charge transfer, as well as line and continuum fluorescence, are all by their nature selective, i.e. they tend to excite a few lines selectively. In contrast, the O II lines observed in the spectrum of NGC 7009 arise from many different multiplets. Accurate measurements of the strengths of these lines can thus provide a unique opportunity to study the radiative recombination processes and to test the accuracy of current recombination theory for non-hydrogenic ions. This has become feasible with the advent of modern linear, high-quantum-efficiency and large-format detectors such as the IPCS and CCD devices.

New effective radiative recombination coefficients for a number of C, N and O ions were presented by Péquignot, Petitjean & Boisson (1991). Using these atomic data, Nikitin et al. (1993; see also Nikitin et al. 1987) derived C, N and O abundances for a large sample of PNe using line intensities taken from the literature (Kaler 1976; Aller & Czyzak 1979, 1983; Aller & Keyes 1987). The resultant abundances were found to be systematically higher than those from the forbidden lines. A much more sophisticated calculation of O II recombination coefficients, utilizing updated atomic data from the Opacity Project, is presented in a recent paper by Storey (1994). Peimbert, Storey & Torres-Peimbert (1993) have used these data to derive the oxygen abundances in two H II regions, M 17 and the Orion nebula, and in the planetary nebula NGC 6572, based on measurements, some photographic, taken from the literature. Again the resultant abundances were found to be systematically higher than those derived from the forbidden lines. Hitherto, all published calculations of effective recombination coefficients for lines from heavier ions were made entirely within the framework of pure LS-coupling. On the other hand, as already noted by Wenåker (1990), LS-coupling breaks down for the O II 4f–3d transitions, transitions which are particularly useful in abundance determination since they are free of optical depth effects.

In this paper, we present new observations of the rich O II recombination spectrum of NGC 7009, using both IPCS and CCD detectors at medium to high resolution (Section 2). Some properties of NGC 7009 derived from the standard plasma diagnostics are given in Section 3. In Section 4, we present new quantal physics calculations of O II radiative recombination coefficients for the 3d–3p and 4f–3d transitions in intermediate coupling. Our line intensity measurements for the O II recombination lines from NGC 7009 are presented in Section 5, and their relative intensities are compared there to the new theoretical calculations. Oxygen abundances based on these recombination lines, as well as those based on the classical forbidden lines are also derived. Our spectra also cover some important C and N recombination lines, which are analysed in Section 6. A brief discussion of the results presented in this paper is given in Section 7. A more extensive discussion of our results will be given in a separate paper, where we extend our observations to additional PNe (Barlow et al. 1995, in preparation). We summarize our results in Section 8.

2 OBSERVATIONS AND DATA REDUCTION

In this section, we describe the new spectrophotometric observations of O II lines in the spectrum of the planetary nebula NGC 7009 and our data reduction techniques. Comments on our measurements of O II recombination lines, using deblending techniques when necessary, will be presented in Section 5.

The observations reported here were obtained during two observing runs in 1979 July and 1981 July at the AAO, Siding Spring, and during a further two observing runs at ESO, La Silla, in 1992 May and 1993 April. An observational journal is presented in Table 1.

In 1979 July and 1981 July, NGC 7009 was observed with the RGO Spectrograph mounted at the Cassegrain focus of the 3.9-m AAT. The 25-cm camera was used, with the IPCS as detector. All the spectra of the nebula were secured with a long slit, whose width could be varied (the slit-widths used are listed in Table 1). The IPCS format was 2048 spectral pixels times 11 spatial increments in 1979 and 2048 × 20 in 1981. On each occasion, an IPCS spatial increment along the slit projected to 2.2 arcsec on the sky. A 1200 line mm^{-1} grating was used which, in combination with the slit-widths used, yielded the FWHM spectral resolutions listed in Table 1. No standard stars were observed in 1979 July, but in 1981 July the white dwarf VMa2 (Oke 1974) was observed for flux calibration purposes.

Observations with the ESO 1.5-m telescope were obtained in 1992 May and 1993 April with the Boller &

Table 1. Observational journal.

Date	Telescope	Wavelength Range (Å)	Slit-width (arcsec)	FWHM (Å)	Exposure Time (sec)	PA	Note
07/07/79	AAT 3.9m	3682–3986	0.94	0.64	1500	45	
07/07/79	AAT 3.9m	4312–4577	0.94	0.74	1467	45	
08/07/79	AAT 3.9m	4146–4633	1.70	0.77	457,1800	60	cloud
08/07/79	AAT 3.9m	3743–4237	1.70	0.77	1401	60	cloud
22/07/81	AAT 3.9m	4250–4715	1.00	0.64	1200	45	
22/07/81	AAT 3.9m	4250–4715	1.00	0.64	200	45	ND1.0
22/07/81	AAT 3.9m	4250–4715	1.00	0.64	100	45	ND1.3
22/07/81	AAT 3.9m	4250–4715	6.70	1.73	350	45	ND0.7
22/07/81	AAT 3.9m	4250–4715	6.70	1.73	100	45	ND1.6
23/04/93	ESO 1.5m	3400–6800	1.50	4.25	180,600	45	
26/04/93	ESO 1.5m	4015–4966	2.00	1.48	1800	45	
13/05/92	ESO 1.5m	3400–6800	1.50	4.25	60,120,600	0	
14/05/92	ESO 1.5m	3400–6800	1.50	4.25	60	0	
15/05/92	ESO 1.5m	4040–5015	1.50	1.08	3 × 1200,120	0	
16/05/92	ESO 1.5m	3707–4695	1.50	1.08	1200	0	
24/04/93	ESO 1.5m	4015–4966	2.00	1.48	1800	0	
25/04/93	ESO 1.5m	4015–4966	2.00	1.48	1500	0	

Chivens spectrograph and a Ford 2048 × 2048 CCD (15-μm pixel size). The plate-scale at the detector was 0.68 arcsec pixel^{-1}. Two gratings were used to provide wavelength coverages of about 3400 and 1000 Å at resolutions of about 4.2 and 1.2 Å, respectively. Whenever necessary, appropriate filters were used to block light from other spectral orders. In 1992, wide-slit (9-arcsec) observations of the standards LTT 4816, EG 274 and LTT 7987 (Stone & Baldwin 1983) and LDS 749B (Oke 1974) were used for flux calibration purposes. In 1993, LDS 749B, L745-46A (Oke 1974) and LTT 7987 (Hamuy et al. 1992) were used. Throughout the observing runs in 1992 and 1993, there were thin clouds. The slit position angles (PAs) are listed in Table 1. In all the cases listed in Table 1, the slit was positioned through the central star.

All the data were reduced and analysed using standard procedures for long-slit spectra. The IPCS data were reduced using the software package FIGARO at the Department of Physics and Astronomy, University College London. The CCD spectra were analysed using the IRAF package at the same site. The raw CCD spectra were flat-fielded, bias- and dark-subtracted and wavelength-calibrated. The sky-background was subtracted by fitting a low-order polynomial column by column to scan lines outside the nebular emission. Pixels affected by cosmic rays were removed by a software median filter. For the IPCS spectra secured in 1979, the small format used provided a total slit-length of only 24.2 arcsec, which was just enough to cover the main part of NGC 7009; no sky background was subtracted. However, the blue wavelength region is relatively clear of strong sky emission lines, and so this has little effect on our measurements. The monochromatic response of the instrument was derived from the spectra of the observed standards. Atmospheric extinction was corrected for using mean extinction curves for the observatories. The flux-calibrated spectra were finally summed along the slit to obtain one-dimensional spectra. To avoid the strong background from the central star, a region of about 4 arcsec in length, centred on the central star, was excluded when summing along the slit.

As mentioned above, no standard stars were observed in 1979 July. To calibrate these spectra, we made use of a low-resolution spectrum of NGC 7009 secured with a 4.1-arcsec wide long-slit centred on the central star, obtained in 1978 October at the AAT using the RGO Spectrograph and IPCS (Kingsburgh & Barlow 1995). A neutral-density filter of 1.78 dex was used to avoid the saturation of Hβ and the [O III] lines. The spectrum covered the wavelength range $\lambda\lambda$3112–7417 and was flux-calibrated with respect to the white dwarf L930-80 (Oke 1974). From this spectrum, after correction for interstellar reddening assuming $c(\mathrm{H}\beta)=0.20$ (Section 3), we derived the absolute monochromatic energy distribution of the central star of NGC 7009. The contribution to the observed continuum from nebular continuum emission was calculated, using recombination theory from the observed fluxes of Hβ, He I $\lambda\lambda$4471, 5876 and 6678 and He II λ4686, and then subtracted. In fact, after the nebular contribution had been subtracted (constituting less than 20 per cent of the total observed continuum flux for $3700<\lambda<5000$ Å), the absolute energy distribution of the central star of NGC 7009 can be well fitted by a Rayleigh–Jeans law with $F_\lambda \propto \lambda^{-4}$. As we were only interested in relative flux calibration, we therefore calibrated our 1979 IPCS spectra of NGC 7009 assuming the dereddened central star in the central pixels to have a Rayleigh–Jeans distribution. The contamination from the nebular continuum emission to the observed continuum (less than 10 per cent due to the much narrower slit-width used in this run) was taken into account and subtracted.

For the spectra obtained in 1979 and 1981, the Hβ line was not covered, and the line intensities were normalized to Hβ via higher order Balmer lines present in the same spectra. It is well known that the IPCS suffers coincidence light loss at high counting rates, so on spectra secured without neutral-density filters, Hγ and sometimes even Hδ and Hε were saturated. For the spectra secured with PA=45°, normalization caused no problems as exposures with high neutral-density filters were also obtained. The only spectra that could not be normalized via Balmer lines were the two secured in 1979 with PA=60°, covering $\lambda\lambda$4146–4633

(Table 1). These two spectra were therefore normalized to Hβ by assuming that the total helium abundance derived from He I λ4471 and He II λ4541 was the same as that derived from the calibrated spectra taken at PA = 45°.

A comparison of the normalized intensities of common O II recombination lines detected in both the PA = 45° and PA = 60° IPCS spectra showed that their intensities do not change significantly with the small change in slit PA, partly due to the geometric symmetry of NGC 7009, and partly due to the fact that the intensities are summed over a long slit. We thus merged the two sets of data to increase the S/N ratio and to obtain more complete wavelength coverage. The very good agreement between the final O II recombination line intensities measured from the IPCS spectra with those measured from the CCD spectra shows that insignificant errors have been introduced by our method of normalizing the IPCS data and merging the spectra secured with the two slit PAs. Hereafter, all IPCS measurements cited refer to those measured on this merged spectrum.

The accuracy of the relative flux calibration is estimated to be about 5 per cent for the CCD data and about 10–15 per cent for the IPCS data. All the O II recombination lines are extremely weak, with typical intensities of 0.05 in units of Hβ = 100 (hereafter all the intensities cited are on this scale). Their observational errors are dominated by the photon-counting noise from the lines themselves, from the sky background, and from the continuum emission of the central star and nebula.

3 PLASMA DIAGNOSTICS

Some properties of NGC 7009 derived from the classic plasma diagnostics are presented in Table 2, including c(Hβ), the logarithmic extinction at Hβ, the electron densities and temperatures derived from a number of forbidden line ratios, the electron temperature deduced from the Balmer discontinuity in the nebular continuum emission, the mean temperature and the temperature fluctuation parameter t^2 (Peimbert 1967) implied by the difference between the Balmer discontinuity temperature and the [O III] forbidden line temperature (Liu & Danziger 1993b), and the ionic and elemental abundances of helium. These parameters will be used later in the paper.

Table 2. Properties of NGC 7009.

Diagnostics	PA=45°	PA=0°
	N_e (cm^{-3})	
[O II] 3729/3726	–	3340
[S II] 6716/6731	4380	3430
[Cl III] 5517/5537	3890	3980
[Ar IV] 4711/4740	4690	4630
Adopted	4300	4000
	T_e (K)	
[O III] (4959+5007)/4363	10060	10180
[N II] (6548+6584)/5754	11760	13990
$\Delta(Bal)/H\beta$	8300	8000
He^+/H^+	0.101	0.0904
He^{2+}/H^+	0.0111	0.0149
He/H	0.113	0.105
T_0 [a] (K)	8850	8670
$t^2(Bal)$ [a]	0.037	0.046
c(Hβ)	0.20	0.20

[a]The mean electron temperature T_0 and temperature fluctuation parameter t^2 are derived from the electron temperatures deduced from the [O III] lines and from the nebular continuum Balmer discontinuity.

The interstellar reddening constant c(Hβ) was derived by comparing the observed Balmer line ratios Hα/Hβ and Hγ/Hβ with the case B values predicted by recombination theory (Hummer & Storey 1987). The interstellar reddening curve from Seaton (1979) has been used. The electron temperatures and densities were derived by solving statistical equilibrium equations for level populations in a five-level atomic model. The atomic data used are the same as those described by Liu & Danziger (1993a). Typical uncertainties are about 500 cm^{-3} in N_e and 500 K in T_e. There is close agreement between the electron densities derived from different diagnostics. For PA = 0°, the electron temperature derived from the [N II] lines is about 3800 K higher than that from the [O III] lines. A similar result was found by Liu & Danziger (1993a) from an independent data set. The electron temperature deduced from the ratio of nebular continuum Balmer discontinuity and Hβ, Δ(Bal)/Hβ, was calculated as described by Liu & Danziger (1993b), and is in good agreement with the result reported in that paper. For both slit angles, the electron temperatures from the ratio of Balmer discontinuity and Hβ are significantly lower than those derived from the [O III] forbidden line ratio, a discrepancy often attributed to the presence of significant temperature fluctuations (Peimbert 1971). The implied mean electron temperature T_0 and the rms temperature fluctuation parameter t^2 are listed in Table 2.

The He^+ abundances were derived from the He I $\lambda\lambda$4471, 5876 and 6678 lines, with weights of 1, 3 and 1, respectively. The effect of collisional excitation and ionization by electron impact are taken into account using the correction factors calculated by Clegg (1987b). The He^{2+} abundances were derived from the He II λ4686 line. In deriving the abundances for both He^+ and He^{2+}, the electron temperature from the [O III] forbidden line ratio has been used. The ionic helium abundances are used later in the paper to compute the ionization correction factors (*icf*s) needed to derive the total abundances from the observed ionic abundances.

4 EFFECTIVE RADIATIVE RECOMBINATION COEFFICIENTS OF O II

The current status of theoretical work on the O II recombination spectrum has been described by Storey (1994), who also gives the results of an elaborate calculation of effective recombination coefficients. His calculations include the best currently available theoretical work on bound–bound and bound–free radiative data for O II, taken from the Opacity Project data base (Cunto et al. 1993), which extends to states with valence electron principal quantum number $n \leq 10$. Also included are the effects of electron and heavy-particle collisions, in a treatment that is valid for $N_e \leq 10^6$ cm^{-3}. These calculations and those of all previous workers were, however, made in LS-coupling and, with a few exceptions, cannot be applied to any states with valence electron orbital angular momentum quantum number $l \geq 3$ (Wenåker 1990). Even for states with $l = 2$, some departures from LS-coupling

occur. It is desirable to make use of transitions arising from high angular momentum states, since they are close to hydrogenic in nature and consequently the atomic data needed to describe them should be reliable.

A fully self-consistent treatment would require that the whole ion be treated in intermediate coupling, in which all the necessary relativistic corrections to the Hamiltonian operator would be included in the calculation of energy levels and dipole matrix elements, and the resulting collisional radiative recombination problem solved. The necessary radiative data are not yet available for such a calculation, but a partial treatment of intermediate coupling effects in some transitions is possible. We consider the levels of the (^{3}P) 4f, (^{3}P) 3d and (^{3}P) 3p electron configurations and make detailed calculations of the radiative transitions between them in intermediate coupling.

We use the general purpose multiconfiguration atomic structure code SUPERSTRUCTURE (Eissner, Jones & Nussbaumer 1974), which incorporates all the fine-structure terms of the Breit–Pauli Hamiltonian. The Hamiltonian is first diagonalized including only electrostatic interactions. Matrix elements of the relativistic interactions (the spin–orbit interaction and other weaker interactions) are calculated in this LS basis. The resulting Hamiltonian is then diagonalized to obtain the eigenvectors of the levels in intermediate coupling as a linear combination of the LS-coupled states. These eigenvectors can then be used to transform LS dipole matrix elements into intermediate coupling. SUPERSTRUCTURE also allows semi-empirical adjustments to be made to the magnitude of individual spin–orbit parameters and to the electrostatic Hamiltonian (Nussbaumer & Storey 1978). This latter adjustment can be used to ensure that term separations are close to their experimental values (Wenåker 1990). *Ab initio* calculations of term separations are often significantly in error unless a very elaborate configuration basis is used to describe the states in question. Accurate term separations are important, since the strength of the mixing of the wave functions of levels from different terms, but with the same total angular momentum quantum number J, depends on these separations.

The configuration basis used to describe the states of interest comprises, for the odd parity states, $2s^22p^3$, $2p^5$, $2s^22p^24f$, $2s^22p^23p$, $2p^44f$, $2p^43p$, and for the even parity states, $2s2p^4$, $2s^22p^23s$, $2s^22p^23d$ and $2p^43d$. The radial wave functions were calculated in scaled statistical model potentials, and the scaling parameters (λ_{nl}) for the potentials are determined by minimizing the energies of the states of interest. Since we are only interested in a good representation of states of the form $2s^22p^2nl$, the scaling parameters for the 1s, 2s and 2p orbitals were determined by minimizing the energies of the $2s^22p^2$ and $2p^4$ terms of the parent ion, O^{2+}. The scaling parameters for the valence orbitals, 4f, 3d and 3p, were then obtained by minimizing the energies of the terms of the $2s^22p^24f$, 3d and 3p configurations. The final values of the scaling parameters were $\lambda_{1s}=1.477\,72$, $\lambda_{2s}=1.228\,89$, $\lambda_{2p}=1.202\,13$, $\lambda_{3s}=1.176\,50$, $\lambda_{3p}=1.148\,37$, $\lambda_{3d}=1.157\,63$ and $\lambda_{4f}=1.096\,69$. For all states, empirical adjustments to the LS term energies were made, and for the 4f orbital the *ab initio* spin–orbit parameter was corrected by a factor of 0.9945. The resulting level energies for the 4f and the 3d configurations are compared with experiment in Table 3. Results are not given for the 3p configuration, since no significant departures from LS-coupling are found. The states are listed in energy order, and energies are given relative to the lowest state in each configuration. We describe the 4f levels in the $L[K]_J$ notation as used by Wenåker (1990) in his measurements of the experimental energies. In this notation, L is the usual quantum number associated with the total orbital angular momentum of the atom. K and J are then obtained by adding successively the total spin of the core electrons and the spin of the valence electron.

From the point of view of calculating accurately the wave functions in intermediate coupling, the important energies are the separations of states of the same J and the magnitude of the relativistic interactions (mainly the spin–orbit interaction) between them. From Table 3, the separations are in error by 1 per cent or less for the 4f states and by up to 4 per cent for the 3d state. The overall accuracy of calculation of the magnitude of the spin–orbit interaction can be judged by comparing the total fine-structure splitting of the individual terms in the 3d configuration with experiment. The largest

Table 3. Comparison of experimental and calculated level energies within the (^{3}P) 4f and (^{3}P) 3d configurations. Energies are given relative to the lowest state in each configuration, in cm^{-1}.

State	Exp.	Cal.
$4f\,D[3]_{5/2}$	0.0	0.0
$4f\,D[3]_{7/2}$	1.4	1.0
$4f\,G[3]_{5/2}$	66.2	66.3
$4f\,G[3]_{7/2}$	69.4	69.5
$4f\,D[2]_{3/2}$	122.7	122.7
$4f\,D[2]_{5/2}$	123.5	123.2
$4f\,G[4]_{9/2}$	137.7	137.7
$4f\,G[4]_{7/2}$	139.6	139.8
$4f\,D[1]_{3/2}$	222.3	221.9
$4f\,D[1]_{1/2}$	222.4	222.4
$4f\,G[5]_{11/2}$	287.5	287.5
$4f\,G[5]_{9/2}$	293.6	294.2
$4f\,F[2]_{3/2}$	393.7	393.3
$4f\,F[2]_{5/2}$	397.8	397.3
$4f\,F[3]_{7/2}$	433.3	432.9
$4f\,F[3]_{5/2}$	435.8	435.4
$4f\,F[4]_{9/2}$	446.1	445.8
$4f\,F[4]_{7/2}$	453.3	452.8
$3d\,^4F_{3/2}$	0.0	0.0
$3d\,^4F_{5/2}$	53.9	54.5
$3d\,^4F_{7/2}$	131.8	133.0
$3d\,^4F_{9/2}$	234.1	236.1
$3d\,^4P_{5/2}$	1166.6	1158.6
$3d\,^4P_{3/2}$	1239.8	1234.2
$3d\,^4P_{1/2}$	1306.4	1303.5
$3d\,^4D_{1/2}$	1415.5	1415.2
$3d\,^4D_{3/2}$	1449.9	1449.6
$3d\,^4D_{5/2}$	1451.4	1453.0
$3d\,^4D_{7/2}$	1457.7	1460.9
$3d\,^2F_{5/2}$	1500.2	1502.0
$3d\,^2F_{7/2}$	1663.1	1665.6
$3d\,^2P_{3/2}$	2134.4	2131.4
$3d\,^2P_{1/2}$	2248.4	2260.5
$3d\,^2D_{3/2}$	3106.7	3105.4
$3d\,^2D_{5/2}$	3158.5	3161.7

error is for the 3d ^{4}D term, where the calculated splitting is too large by about 8 per cent. For the states of the 4f configuration, the calculated positions are in excellent agreement with experiment in all cases. These structure calculations confirm that LS-coupling is completely inappropriate to describe the levels of the 4f configuration. Among the terms of the 3d configuration, the calculations show that there is strong mixing of the wave functions of the levels of the ^{4}P, ^{4}D and ^{2}F terms. The ^{4}F, ^{2}P and ^{2}D terms, on the other hand, are accurately described by LS-coupling.

The intermediate coupling eigenvectors obtained from the above structure calculation were then used to transform the Opacity Project LS-coupled dipole matrix elements. A further complication arose here, in that the Opacity Project archived oscillator strength, rather than matrix elements, so that the signs of the matrix elements were lost. The necessary signs were taken from the dipole matrix elements calculated by the program SUPERSTRUCTURE. Tables 4(a) and 4(b) give the branching ratios from each upper state of the 4f and the 3d configurations, respectively. In Table 4(b), branching ratios are given for three cases, A, B and C. We follow the definition of Peimbert et al. (1993) for these cases. In case A, all emission lines are assumed to be optically thin. In case B, lines terminating on the $2s^22p^3\,{}^4S^\circ$ term are assumed to be thick and no radiative decays are permitted to this state. In case C, radiative decays to both $2s^22p^3\,{}^4S^\circ$ and $^2D^\circ$ are excluded. For the 4f levels, there are no significant radiative decays to levels of the ground configuration, so the branching ratios are insensitive to optical depth effects. Some of the 3d levels can decay directly to terms of the $2s^22p^3$ configuration, so there is case sensitivity. Of particular interest are the levels of the 3d ^{4}D term, which in LS-coupling cannot decay to states in the ground configuration. In intermediate coupling, however, their interaction with levels of 3d ^{4}P and ^{2}F allows this, and the results become case-sensitive. In addition, the branching ratios to levels in the 3p configuration are reduced over their LS-coupled values, even in case A.

To obtain effective recombination coefficients for individual lines, the intermediate coupling radiative data given in Tables 4(a) and 4(b) can be combined with the recombination calculation described by Storey (1994). We assume that the overall population rate of the levels of the $2s^22p^24f$ and 3d configurations does not depend on coupling scheme. In practice, even in LS-coupling, the population rate of the 4f levels, due to direct recombination and cascades, is almost exactly proportional to their statistical weights, $(2J+1)$. The effect of introducing intermediate coupling is to redistribute the cascading further. For the states of the 4f configuration, we have therefore averaged the overall population rate over all levels. For the states of the 3d configuration, we take the population rates of the ^{4}F, ^{2}P and ^{2}D terms to be as given by Storey (1994). These terms are all described by LS-coupling. For the remaining terms, ^{4}P, ^{4}D and ^{2}F, where LS-coupling breaks down, we add the rates of population as calculated by Storey (1994), and assume that the total is equally divided among all quantum states. As in Storey (1994), the effective recombination coefficient is then fitted to a simple function of temperature,

$$\alpha = 10^{-14} a t^b [1 + c(1-t) + d(1-t)^2], \qquad (1)$$

where $t = T_e/10^4$ K, and a, b, c and d are constants. In this scheme, the value of a is just $\alpha \times 10^{14}$ at $t = 1$. Fits for dif-

Table 4. (a) Branching ratios, B, for 4f–3d transitions.

Transition			λ[Å]	B
4f G[5]$_{11/2}$	–	3d ^{4}F$_{9/2}$	4089.29	1.00
4f G[5]$_{9/2}$	–	3d ^{4}F$_{9/2}$	4088.27	.023
4f G[5]$_{9/2}$	–	3d ^{4}F$_{7/2}$	4071.24	.204
4f G[5]$_{9/2}$	–	3d ^{2}F$_{7/2}$	4342.01	.702
4f G[5]$_{9/2}$	–	3d ^{4}D$_{7/2}$	4303.61	.072
4f G[4]$_{9/2}$	–	3d ^{4}F$_{9/2}$	4114.51	.019
4f G[4]$_{9/2}$	–	3d ^{4}F$_{7/2}$	4097.26	.735
4f G[4]$_{9/2}$	–	3d ^{2}F$_{7/2}$	4371.62	.125
4f G[4]$_{9/2}$	–	3d ^{4}D$_{7/2}$	4332.70	.121
4f G[4]$_{7/2}$	–	3d ^{4}F$_{7/2}$	4096.94	.046
4f G[4]$_{7/2}$	–	3d ^{4}F$_{5/2}$	4083.90	.428
4f G[4]$_{7/2}$	–	3d ^{2}F$_{5/2}$	4340.33	.354
4f G[4]$_{7/2}$	–	3d ^{4}D$_{5/2}$	4331.17	.123
4f G[4]$_{7/2}$	–	3d ^{2}D$_{5/2}$	4677.07	.046
4f G[3]$_{7/2}$	–	3d ^{4}F$_{7/2}$	4108.76	.054
4f G[3]$_{7/2}$	–	3d ^{4}D$_{7/2}$	4345.56	.050
4f G[3]$_{7/2}$	–	3d ^{4}F$_{5/2}$	4095.64	.296
4f G[3]$_{7/2}$	–	3d ^{2}F$_{5/2}$	4353.59	.162
4f G[3]$_{7/2}$	–	3d ^{4}D$_{5/2}$	4344.38	.189
4f G[3]$_{7/2}$	–	3d ^{4}P$_{5/2}$	4291.26	.246
4f G[3]$_{5/2}$	–	3d ^{4}F$_{5/2}$	4096.19	.096
4f G[3]$_{5/2}$	–	3d ^{2}F$_{5/2}$	4354.21	.007
4f G[3]$_{5/2}$	–	3d ^{4}D$_{5/2}$	4344.99	.006
4f G[3]$_{5/2}$	–	3d ^{2}D$_{5/2}$	4693.19	.034
4f G[3]$_{5/2}$	–	3d ^{4}P$_{5/2}$	4291.86	.014
4f G[3]$_{5/2}$	–	3d ^{4}F$_{3/2}$	4087.16	.542
4f G[3]$_{5/2}$	–	3d ^{4}P$_{3/2}$	4305.39	.065
4f G[3]$_{5/2}$	–	3d ^{2}P$_{3/2}$	4477.91	.188
4f F[4]$_{9/2}$	–	3d ^{4}F$_{9/2}$	4062.93	.150
4f F[4]$_{9/2}$	–	3d ^{4}F$_{7/2}$	4046.12	.015
4f F[4]$_{9/2}$	–	3d ^{2}F$_{7/2}$	4313.44	.153
4f F[4]$_{9/2}$	–	3d ^{4}D$_{7/2}$	4275.55	.681
4f F[4]$_{7/2}$	–	3d ^{4}F$_{7/2}$	4044.95	.024
4f F[4]$_{7/2}$	–	3d ^{2}F$_{7/2}$	4312.11	.098
4f F[4]$_{7/2}$	–	3d ^{4}D$_{7/2}$	4274.25	.035
4f F[4]$_{7/2}$	–	3d ^{4}F$_{5/2}$	4032.24	.017
4f F[4]$_{7/2}$	–	3d ^{4}D$_{5/2}$	4273.10	.081
4f F[4]$_{7/2}$	–	3d ^{2}D$_{5/2}$	4609.43	.725
4f F[4]$_{7/2}$	–	3d ^{4}P$_{5/2}$	4221.70	.017
4f F[3]$_{7/2}$	–	3d ^{4}F$_{9/2}$	4065.05	.016
4f F[3]$_{7/2}$	–	3d ^{4}F$_{7/2}$	4048.22	.094
4f F[3]$_{7/2}$	–	3d ^{2}F$_{7/2}$	4315.83	.046
4f F[3]$_{7/2}$	–	3d ^{4}D$_{7/2}$	4277.89	.154
4f F[3]$_{7/2}$	–	3d ^{2}F$_{5/2}$	4285.68	.298
4f F[3]$_{7/2}$	–	3d ^{4}D$_{5/2}$	4276.75	.315
4f F[3]$_{7/2}$	–	3d ^{2}D$_{5/2}$	4613.68	.074
4f F[3]$_{5/2}$	–	3d ^{4}F$_{7/2}$	4047.80	.011
4f F[3]$_{5/2}$	–	3d ^{4}D$_{7/2}$	4277.43	.010
4f F[3]$_{5/2}$	–	3d ^{4}F$_{5/2}$	4035.07	.052
4f F[3]$_{5/2}$	–	3d ^{4}D$_{5/2}$	4276.29	.158
4f F[3]$_{5/2}$	–	3d ^{2}D$_{5/2}$	4613.14	.077
4f F[3]$_{5/2}$	–	3d ^{4}P$_{5/2}$	4224.81	.006
4f F[3]$_{5/2}$	–	3d ^{4}F$_{3/2}$	4026.31	.010
4f F[3]$_{5/2}$	–	3d ^{4}D$_{3/2}$	4276.00	.218
4f F[3]$_{5/2}$	–	3d ^{2}D$_{3/2}$	4602.13	.385
4f F[3]$_{5/2}$	–	3d ^{4}P$_{3/2}$	4237.92	.022
4f F[3]$_{5/2}$	–	3d ^{2}P$_{3/2}$	4404.97	.037
4f F[2]$_{5/2}$	–	3d ^{4}F$_{7/2}$	4054.04	.014
4f F[2]$_{5/2}$	–	3d ^{2}F$_{7/2}$	4322.45	.007
4f F[2]$_{5/2}$	–	3d ^{4}D$_{7/2}$	4284.40	.012
4f F[2]$_{5/2}$	–	3d ^{4}F$_{5/2}$	4041.27	.033
4f F[2]$_{5/2}$	–	3d ^{2}F$_{5/2}$	4292.21	.186

Table 4 – *continued*

(a) Transition			λ[Å]	B
$4f\,F[2]_{5/2}$	–	$3d\,^4D_{5/2}$	4283.25	.065
$4f\,F[2]_{5/2}$	–	$3d\,^2D_{5/2}$	4621.24	.043
$4f\,F[2]_{5/2}$	–	$3d\,^4D_{3/2}$	4282.96	.323
$4f\,F[2]_{5/2}$	–	$3d\,^2D_{3/2}$	4610.20	.306
$4f\,F[2]_{3/2}$	–	$3d\,^4F_{5/2}$	4041.95	.021
$4f\,F[2]_{3/2}$	–	$3d\,^2F_{5/2}$	4292.98	.011
$4f\,F[2]_{3/2}$	–	$3d\,^4D_{5/2}$	4284.01	.029
$4f\,F[2]_{3/2}$	–	$3d\,^4F_{3/2}$	4033.16	.063
$4f\,F[2]_{3/2}$	–	$3d\,^4D_{3/2}$	4283.72	.302
$4f\,F[2]_{3/2}$	–	$3d\,^2D_{3/2}$	4611.08	.012
$4f\,F[2]_{3/2}$	–	$3d\,^4P_{3/2}$	4245.51	.009
$4f\,F[2]_{3/2}$	–	$3d\,^2P_{3/2}$	4413.17	.012
$4f\,F[2]_{3/2}$	–	$3d\,^4D_{1/2}$	4277.43	.419
$4f\,F[2]_{3/2}$	–	$3d\,^4P_{1/2}$	4257.54	.047
$4f\,F[2]_{3/2}$	–	$3d\,^2P_{1/2}$	4435.50	.062
$4f\,D[3]_{7/2}$	–	$3d\,^4D_{7/2}$	4358.44	.026
$4f\,D[3]_{7/2}$	–	$3d\,^4F_{5/2}$	4107.09	.173
$4f\,D[3]_{7/2}$	–	$3d\,^2F_{5/2}$	4366.53	.050
$4f\,D[3]_{7/2}$	–	$3d\,^4D_{5/2}$	4357.25	.079
$4f\,D[3]_{7/2}$	–	$3d\,^2D_{5/2}$	4707.50	.014
$4f\,D[3]_{7/2}$	–	$3d\,^4P_{5/2}$	4303.82	.652
$4f\,D[3]_{5/2}$	–	$3d\,^4F_{5/2}$	4107.33	.016
$4f\,D[3]_{5/2}$	–	$3d\,^2F_{5/2}$	4366.80	.009
$4f\,D[3]_{5/2}$	–	$3d\,^2D_{5/2}$	4707.82	.032
$4f\,D[3]_{5/2}$	–	$3d\,^4P_{5/2}$	4304.09	.032
$4f\,D[3]_{5/2}$	–	$3d\,^4F_{3/2}$	4098.25	.333
$4f\,D[3]_{5/2}$	–	$3d\,^4D_{3/2}$	4357.23	.016
$4f\,D[3]_{5/2}$	–	$3d\,^2D_{3/2}$	4696.36	.041
$4f\,D[3]_{5/2}$	–	$3d\,^4P_{3/2}$	4317.70	.150
$4f\,D[3]_{5/2}$	–	$3d\,^2P_{3/2}$	4491.22	.301
$4f\,D[2]_{5/2}$	–	$3d\,^4D_{7/2}$	4335.36	.013
$4f\,D[2]_{5/2}$	–	$3d\,^4F_{5/2}$	4086.59	.010
$4f\,D[2]_{5/2}$	–	$3d\,^2F_{5/2}$	4343.36	.006
$4f\,D[2]_{5/2}$	–	$3d\,^4D_{5/2}$	4334.19	.077
$4f\,D[2]_{5/2}$	–	$3d\,^2D_{5/2}$	4680.59	.012
$4f\,D[2]_{5/2}$	–	$3d\,^4P_{5/2}$	4281.32	.111
$4f\,D[2]_{5/2}$	–	$3d\,^2D_{3/2}$	4669.26	.051
$4f\,D[2]_{5/2}$	–	$3d\,^4P_{3/2}$	4294.79	.487
$4f\,D[2]_{5/2}$	–	$3d\,^2P_{3/2}$	4466.44	.199
$4f\,D[2]_{3/2}$	–	$3d\,^4D_{5/2}$	4334.33	.021
$4f\,D[2]_{3/2}$	–	$3d\,^2D_{5/2}$	4680.76	.006
$4f\,D[2]_{3/2}$	–	$3d\,^4P_{5/2}$	4281.46	.008
$4f\,D[2]_{3/2}$	–	$3d\,^4F_{3/2}$	4077.73	.017
$4f\,D[2]_{3/2}$	–	$3d\,^4D_{3/2}$	4334.04	.032
$4f\,D[2]_{3/2}$	–	$3d\,^2D_{3/2}$	4669.43	.062
$4f\,D[2]_{3/2}$	–	$3d\,^4P_{3/2}$	4294.93	.172
$4f\,D[2]_{3/2}$	–	$3d\,^2P_{3/2}$	4466.59	.035
$4f\,D[2]_{3/2}$	–	$3d\,^4D_{1/2}$	4327.59	.031
$4f\,D[2]_{3/2}$	–	$3d\,^4P_{1/2}$	4307.24	.331
$4f\,D[2]_{3/2}$	–	$3d\,^2P_{1/2}$	4489.47	.215
$4f\,D[1]_{3/2}$	–	$3d\,^2F_{5/2}$	4324.78	.025
$4f\,D[1]_{3/2}$	–	$3d\,^4D_{5/2}$	4315.68	.019
$4f\,D[1]_{3/2}$	–	$3d\,^2D_{5/2}$	4659.02	.008
$4f\,D[1]_{3/2}$	–	$3d\,^4P_{5/2}$	4263.26	.006
$4f\,D[1]_{3/2}$	–	$3d\,^4D_{3/2}$	4315.39	.148
$4f\,D[1]_{3/2}$	–	$3d\,^2D_{3/2}$	4647.79	.079
$4f\,D[1]_{3/2}$	–	$3d\,^4P_{3/2}$	4276.61	.100
$4f\,D[1]_{3/2}$	–	$3d\,^2P_{3/2}$	4446.78	.048
$4f\,D[1]_{3/2}$	–	$3d\,^4D_{1/2}$	4309.00	.018
$4f\,D[1]_{3/2}$	–	$3d\,^4P_{1/2}$	4288.82	.153
$4f\,D[1]_{3/2}$	–	$3d\,^2P_{1/2}$	4469.46	.317
$4f\,D[1]_{1/2}$	–	$3d\,^4D_{3/2}$	4315.33	.179
$4f\,D[1]_{1/2}$	–	$3d\,^4P_{3/2}$	4276.56	.040
$4f\,D[1]_{1/2}$	–	$3d\,^4D_{1/2}$	4308.94	.455
$4f\,D[1]_{1/2}$	–	$3d\,^4P_{1/2}$	4288.76	.323

Table 4. (b) Branching ratios for 3d–3p transitions.

Transition			λ[Å]	Case A	Case B	Case C
$3d\,^4F_{9/2}$	–	$3p\,^4D_{7/2}$	4075.86	1.00	1.00	1.00
$3d\,^4F_{7/2}$	–	$3p\,^4D_{7/2}$	4092.93	.118	.118	.120
$3d\,^4F_{7/2}$	–	$3p\,^4D_{5/2}$	4072.15	.865	.865	.879
$3d\,^4F_{5/2}$	–	$3p\,^4D_{7/2}$	4106.02	.007	.007	.007
$3d\,^4F_{5/2}$	–	$3p\,^4D_{5/2}$	4085.12	.216	.216	.219
$3d\,^4F_{5/2}$	–	$3p\,^4D_{3/2}$	4069.89	.760	.761	.772
$3d\,^4F_{3/2}$	–	$3p\,^4D_{5/2}$	4094.14	.016	.016	.016
$3d\,^4F_{3/2}$	–	$3p\,^4D_{3/2}$	4078.84	.263	.264	.264
$3d\,^4F_{3/2}$	–	$3p\,^4D_{1/2}$	4069.62	.715	.715	.716
$3d\,^4D_{7/2}$	–	$3p\,^4D_{7/2}$	3882.19	.137	.137	.248
$3d\,^4D_{7/2}$	–	$3p\,^4D_{5/2}$	3863.50	.016	.016	.028
$3d\,^4D_{7/2}$	–	$3p\,^2D_{5/2}$	4751.28	.021	.021	.038
$3d\,^4D_{7/2}$	–	$3p\,^4P_{5/2}$	4119.22	.378	.378	.686
$3d\,^4D_{5/2}$	–	$3p\,^4D_{7/2}$	3883.13	.005	.006	.043
$3d\,^4D_{5/2}$	–	$3p\,^4D_{5/2}$	3864.43	.009	.012	.086
$3d\,^4D_{5/2}$	–	$3p\,^2D_{5/2}$	4752.69	.002	.002	.015
$3d\,^4D_{5/2}$	–	$3p\,^4P_{5/2}$	4120.28	.034	.045	.312
$3d\,^4D_{5/2}$	–	$3p\,^4D_{3/2}$	3850.80	.002	.003	.022
$3d\,^4D_{5/2}$	–	$3p\,^2D_{3/2}$	4710.01	.034	.045	.313
$3d\,^4D_{5/2}$	–	$3p\,^4P_{3/2}$	4104.72	.018	.024	.167
$3d\,^4D_{5/2}$	–	$3p\,^4S_{3/2}$	4856.39	.004	.005	.037
$3d\,^4D_{3/2}$	–	$3p\,^4D_{5/2}$	3864.67	.015	.089	.091
$3d\,^4D_{3/2}$	–	$3p\,^4P_{5/2}$	4120.55	.027	.163	.166
$3d\,^4D_{3/2}$	–	$3p\,^4D_{3/2}$	3851.03	.011	.065	.066
$3d\,^4D_{3/2}$	–	$3p\,^4P_{3/2}$	4104.99	.076	.450	.459
$3d\,^4D_{3/2}$	–	$3p\,^4S_{3/2}$	4856.76	.013	.079	.081
$3d\,^4D_{3/2}$	–	$3p\,^4D_{1/2}$	3842.81	.007	.039	.039
$3d\,^4D_{3/2}$	–	$3p\,^4P_{1/2}$	4097.22	.011	.068	.069
$3d\,^4D_{1/2}$	–	$3p\,^4D_{3/2}$	3856.13	.014	.104	.107
$3d\,^4D_{1/2}$	–	$3p\,^4P_{3/2}$	4110.79	.056	.410	.423
$3d\,^4D_{1/2}$	–	$3p\,^4S_{3/2}$	4864.88	.014	.099	.102
$3d\,^4D_{1/2}$	–	$3p\,^4D_{1/2}$	3847.89	.009	.067	.069
$3d\,^4D_{1/2}$	–	$3p\,^4P_{1/2}$	4103.00	.034	.248	.256
$3d\,^4P_{5/2}$	–	$3p\,^4D_{5/2}$	3907.46	.002	.054	.056
$3d\,^4P_{5/2}$	–	$3p\,^4P_{5/2}$	4169.22	.007	.153	.159
$3d\,^4P_{5/2}$	–	$3p\,^4D_{3/2}$	3893.52	.001	.013	.013
$3d\,^4P_{5/2}$	–	$3p\,^4P_{3/2}$	4153.30	.020	.449	.465
$3d\,^4P_{5/2}$	–	$3p\,^4S_{3/2}$	4924.53	.013	.289	.300
$3d\,^4P_{3/2}$	–	$3p\,^4D_{5/2}$	3896.30	.001	.010	.010
$3d\,^4P_{3/2}$	–	$3p\,^4P_{5/2}$	4156.53	.006	.107	.111
$3d\,^4P_{3/2}$	–	$3p\,^4D_{3/2}$	3882.44	.003	.053	.055
$3d\,^4P_{3/2}$	–	$3p\,^4P_{3/2}$	4140.70	.001	.010	.011
$3d\,^4P_{3/2}$	–	$3p\,^4S_{3/2}$	4906.83	.013	.254	.264
$3d\,^4P_{3/2}$	–	$3p\,^4D_{1/2}$	3874.09	.001	.022	.023
$3d\,^4P_{3/2}$	–	$3p\,^4P_{1/2}$	4132.80	.025	.469	.486
$3d\,^4P_{1/2}$	–	$3p\,^4D_{3/2}$	3872.44	.002	.026	.027
$3d\,^4P_{1/2}$	–	$3p\,^4P_{3/2}$	4129.32	.007	.112	.117
$3d\,^4P_{1/2}$	–	$3p\,^4S_{3/2}$	4890.86	.014	.236	.246
$3d\,^4P_{1/2}$	–	$3p\,^4D_{1/2}$	3864.13	.004	.066	.069
$3d\,^4P_{1/2}$	–	$3p\,^4P_{1/2}$	4121.46	.028	.479	.498
$3d\,^2F_{7/2}$	–	$3p\,^4D_{7/2}$	3851.47	.001	.001	.021
$3d\,^2F_{7/2}$	–	$3p\,^4D_{5/2}$	3833.07	.000	.000	.008
$3d\,^2F_{7/2}$	–	$3p\,^2D_{5/2}$	4705.35	.055	.055	.916
$3d\,^2F_{7/2}$	–	$3p\,^4P_{5/2}$	4084.65	.003	.003	.055
$3d\,^2F_{5/2}$	–	$3p\,^4D_{7/2}$	3875.80	.003	.003	.032
$3d\,^2F_{5/2}$	–	$3p\,^4D_{5/2}$	3857.17	.006	.007	.064
$3d\,^2F_{5/2}$	–	$3p\,^2D_{5/2}$	4741.71	.003	.003	.029
$3d\,^2F_{5/2}$	–	$3p\,^4P_{5/2}$	4112.02	.020	.022	.211
$3d\,^2F_{5/2}$	–	$3p\,^4D_{3/2}$	3843.58	.003	.003	.031
$3d\,^2F_{5/2}$	–	$3p\,^2D_{3/2}$	4699.22	.044	.049	.461
$3d\,^2F_{5/2}$	–	$3p\,^4P_{3/2}$	4096.53	.014	.016	.151
$3d\,^2F_{5/2}$	–	$3p\,^4S_{3/2}$	4844.92	.002	.002	.017

Table 4 – *continued*

(b) Transition			λ[Å]	Case A	Case B	Case C
$3d\,^2D_{5/2}$	–	$3p\,^2D_{5/2}$	4395.94	.016	.016	.022
$3d\,^2D_{5/2}$	–	$3p\,^2P_{3/2}$	4943.00	.038	.038	.053
$3d\,^2D_{3/2}$	–	$3p\,^2D_{3/2}$	4369.27	.014	.014	.020
$3d\,^2D_{3/2}$	–	$3p\,^2P_{3/2}$	4955.70	.009	.009	.012
$3d\,^2D_{3/2}$	–	$3p\,^2P_{1/2}$	4941.07	.029	.029	.040
$3d\,^2P_{3/2}$	–	$3p\,^2P_{3/2}$	5206.64	.011	.011	.019
$3d\,^2P_{3/2}$	–	$3p\,^2P_{1/2}$	5190.50	.004	.004	.006
$3d\,^2P_{3/2}$	–	$3p\,^2S_{1/2}$	3390.21	.027	.027	.050
$3d\,^2P_{1/2}$	–	$3p\,^2P_{3/2}$	5175.90	.005	.005	.009
$3d\,^2P_{1/2}$	–	$3p\,^2P_{1/2}$	5159.94	.010	.010	.018
$3d\,^2P_{1/2}$	–	$3p\,^2S_{1/2}$	3377.15	.026	.026	.049

ferent densities and cases can be obtained by taking the appropriate value of a from Table 5(a). With an error of no more than 2 per cent, the same fit to the temperature variation of the recombination coefficients can be used for all densities and cases. The fit coefficients b, c and d are given in Table 5(b). The application of equation (1) with the data in Tables 5(a) and 5(b) will yield the effective recombination *per quantum state*. The effective recombination coefficient for a given level is then given by

$$\alpha(J) = (2J+1)\,\alpha, \tag{2}$$

and the effective recombination for a particular line $J \rightarrow J'$ is given by

$$\alpha(J, J') = (2J+1)\,B(J, J')\,\alpha, \tag{3}$$

where the branching ratios $B(J, J')$ are given in Tables 4(a) and 4(b).

Table 5. (a) Values of the fit parameter a as a function of case and electron density, N_e.

State	Case	$N_e[cm^{-3}] = 10^2$	10^4	10^5	10^6
all 4f	A	.236	.232	.228	.222
$3d\,^4F$	A	.876	.876	.877	.880
$3d\,^4D$	A	.727	.726	.725	.726
	B	.747	.745	.744	.745
	C	.769	.767	.766	.766
$3d\,^4P$	A	.727	.726	.725	.726
	B	.747	.745	.744	.745
	C	.769	.767	.766	.766
$3d\,^2F$	A	.727	.726	.725	.726
	B	.747	.745	.744	.745
	C	.769	.767	.766	.766
$3d\,^2D$	A	.603	.601	.600	.599
	C	.620	.618	.616	.615
$3d\,^2P$	A	.526	.524	.523	.524
	C	.538	.536	.535	.536

Table 5. (b) Values of the fit parameters b, c and d.

State	b	c	d
all 4f	-0.92009	0.15526	0.03442
$3d\,^4F$	-0.73465	0.13689	0.06220
$3d\,^4D$	-0.74621	0.15710	0.07059
$3d\,^4P$	-0.74621	0.15710	0.07059
$3d\,^2F$	-0.74621	0.15710	0.07059
$3d\,^2D$	-0.79533	0.15314	0.05322
$3d\,^2P$	-0.78448	0.13681	0.05608

5 THE O II RECOMBINATION SPECTRUM OF NGC 7009

In Section 5.1, the observed intensities of O II recombination lines from NGC 7009 are presented, together with some detailed comments on individual multiplets. Examples illustrating the techniques used to retrieve the intensities of blended lines are given. The results are compared to the theoretical predictions for LS-coupling as well as for intermediate coupling. Abundance determinations and a further comparison between observations and recombination theory are presented in Section 5.2. Finally, in the last part of this section, we present our adopted O^{2+} abundance derived from the recombination lines and calculate the total oxygen abundance using the empirical *icf* method. The ionic and total oxygen abundances deduced from the forbidden lines are also presented here, for comparison purposes.

Although the discussion in this section is based on observations of NGC 7009, most of the comments apply to the other PNe analysed by Barlow et al. (1995, in preparation). When necessary, some results from objects analysed in that paper will be cited to support arguments.

5.1 Line intensities

The strengths of the O II recombination lines identified and measured in the spectrum of NGC 7009, after correction for interstellar reddening, are presented in Tables 6(a) and 6(b). Columns 1–3 list the wavelengths, the multiplet numbers as assigned in the RMT (Moore 1972) and the transitions. The wavelengths and level notation are taken from Wenåker (1990). For the s, p and d levels, LS symbols are used, whereas, for the f levels, the $L[K]_J$ notation described in the last section is adopted. When a measured feature is a blend of several transitions, only the wavelength and transition of the strongest component are listed; others are in notes at the end of Table 6(b). The succeeding columns in Table 6 list the dereddened relative line intensities and the ionic abundances of O^{2+} derived from them (Section 5.2), for the three different cases. The accuracy of a given line intensity depends on the spectral region in which the line is located and whether it is blended with other lines. It is difficult to give a uniform estimate. Roughly speaking, the intensities of the strongest lines listed are estimated to be accurate to 15 per cent; others are accurate to about 30 per cent, except the very weakest and those marked with a colon, which may be in error by a factor of 2 or more.

All the levels listed in Table 6 are built on ^3P parentage, the ground term of O^{2+}. These include three multiplets from the 3p–3s transitions, four multiplets from the 3d–3p transitions and dozens of transitions from the 4f–3d group. In addition to the lines listed in Table 6, a few transitions from Rydberg states of parentage other than ^3P have been observed in the spectrum of NGC 7009. They are listed in Table 7, and will not be discussed further in this paper. We

Table 6. (a) Optical O II recombination lines in NGC 7009 (3–3 transitions).

Wavelength (Å)	MT	Transition	Slit PA=0° CCD Spectra Intensity (Hβ=100)		O^{2+}/H^+ (10^{-3}) A	B	C	Slit PA=45° IPCS Spectra Intensity (Hβ=100)		O^{2+}/H^+ (10^{-3}) A	B	C	Slit PA=45° CCD Spectra Intensity (Hβ=100)		O^{2+}/H^+ (10^{-3}) A	B	C	Note
4638.86	1	$3p\,^4D_{3/2}-3s\,^4P_{1/2}$	0.457					0.271					0.381					(1)
4641.82	1	$3p\,^4D_{5/2}-3s\,^4P_{3/2}$	0.450					0.334					0.404					(2)
4649.14	1	$3p\,^4D_{7/2}-3s\,^4P_{5/2}$	0.659	*	1.36	1.31		0.617	*	1.27	1.23		0.614	*	1.26	1.22		
4650.84	1	$3p\,^4D_{1/2}-3s\,^4P_{1/2}$	0.189	*	1.86	1.79		0.155	*	1.53	1.47		0.148	*	1.46	1.40		
4661.63	1	$3p\,^4D_{3/2}-3s\,^4P_{3/2}$	0.202	*	1.56	1.50		0.188	*	1.45	1.40		0.196	*	1.51	1.46		
4673.74	1	$3p\,^4D_{1/2}-3s\,^4P_{3/2}$	0.0720	*	3.56	3.43		0.0443	*	2.19	2.11		0.0580	*	2.87	2.76		
4676.24	1	$3p\,^4D_{5/2}-3s\,^4P_{5/2}$	0.173	*	1.58	1.53		0.138	*	1.26	1.22		0.147	*	1.34	1.30		
M 1			**1.86**		**1.53**	**1.47**		**1.64**		**1.35**	**1.30**		**1.67**		**1.37**	**1.32**		(3)
4317.14	2	$3p\,^4P_{3/2}-3s\,^4P_{1/2}$	0.0722	*	1.34	0.96		0.105	*	1.95	1.39		0.0890	*	1.65	1.18		
4319.63	2	$3p\,^4P_{5/2}-3s\,^4P_{3/2}$	0.0353	*	0.60	0.43		0.0752	*	1.29	0.92		0.0492	*	0.84	0.60		
4325.16	2	$3p\,^4P_{1/2}-3s\,^4P_{1/2}$	0.0110:	*	1.02	0.73		0.0206:	*	1.92	1.36		0.0301	*	2.80	1.999		
4345.56	2	$3p\,^4P_{1/2}-3s\,^4P_{3/2}$	0.0597					0.146					0.123:					(4)
4349.43	2	$3p\,^4P_{5/2}-3s\,^4P_{5/2}$	0.134	*	0.99	0.70		0.181	*	1.34	0.95		0.193	*	1.43	1.01		
4366.89	2	$3p\,^4P_{3/2}-3s\,^4P_{5/2}$	0.0555					0.156					0.0911:					(5)
M 2			**0.379**		**0.98**	**0.69**		**0.573**		**1.48**	**1.05**		**0.541**		**1.40**	**0.99**		(3)
4414.90	5	$3p\,^2D_{5/2}-3s\,^2P_{3/2}$	0.0734	*	1.40		0.23	0.0799	*	1.52		0.25	0.101	*	1.52		0.25	
4416.97	5	$3p\,^2D_{3/2}-3s\,^2P_{1/2}$	0.0594	*	2.03		0.33	0.0591	*	2.02		0.33	0.0714	*	2.02		0.33	
4452.37	5	$3p\,^2D_{3/2}-3s\,^2P_{3/2}$	0.0209:	*	3.56		0.59	0.0148:	*	2.52		0.42						
M 5			**0.154**		**1.76**		**0.29**	**0.154**		**1.76**		**0.29**	**0.185**		**2.11**		**0.35**	(3)
4069.89	10	$3d\,^4F_{5/2}-3p\,^4D_{3/2}$	0.621					0.514					0.680					(6)
4072.16	10	$3d\,^4F_{7/2}-3p\,^4D_{5/2}$	0.506	*	2.10	2.10	2.07	0.438	*	1.82	1.82	1.79	0.515	*	2.14	2.14	2.11	
4075.86	10	$3d\,^4F_{9/2}-3p\,^4D_{7/2}$	0.534					0.576					0.649					(7)
4078.84	10	$3d\,^4F_{3/2}-3p\,^4D_{3/2}$	0.0458	*	1.25	1.25	1.25	0.0482	*	1.32	1.32	1.31	0.0604	*	1.65	1.65	1.65	
4085.11	10	$3d\,^4F_{5/2}-3p\,^4D_{5/2}$	0.0800	*	1.78	1.78	1.76	0.0660	*	1.47	1.47	1.45	0.0768	*	1.71	1.71	1.68	
4092.94	10	$3d\,^4F_{7/2}-3p\,^4D_{7/2}$	0.0418:		1.27	1.27	1.25	0.0516:		1.57	1.57	1.55	0.0427:		1.30	1.30	1.28	
4094.14	10	$3d\,^4F_{3/2}-3p\,^4D_{5/2}$						0.0455:										(8)
Sum			**0.632**		**1.96**	**1.96**	**1.93**	**0.552**		**1.72**	**1.72**	**1.69**	**0.652**		**2.03**	**2.03**	**2.00**	(9)
3882.19	12	$3d\,^4D_{7/2}-3p\,^4D_{7/2}$	**0.0593**	*	**1.75**	**1.69**	**0.83**	**0.0623**	*	**1.84**	**1.77**	**0.87**						(10)
4132.80	19	$3d\,^4P_{3/2}-3p\,^4P_{1/2}$	0.0466:		16.7	0.85	0.80	0.0274:		9.82	0.50	0.47						
4153.30	19	$3d\,^4P_{5/2}-3p\,^4P_{3/2}$	0.0942	*	28.1	1.21	1.13	0.0800	*	23.8	1.02	0.96	0.110	*	32.8	1.41	1.32	
4156.53	19	$3d\,^4P_{3/2}-3p\,^4P_{5/2}$	0.0783	*	123.	6.30	5.90	0.0567	*	89.3	4.56	4.27	0.0934	*	147.	7.51	7.03	
4169.22	19	$3d\,^4P_{5/2}-3p\,^4P_{5/2}$	0.0566	*	49.6	2.13	2.00	0.0547	*	48.0	2.06	1.93	0.0668	*	58.6	2.52	2.36	
Sum			**0.229**		**44.8**	**2.01**	**1.94**	**0.191**		**37.4**	**1.68**	**1.62**	**0.270**		**52.9**	**2.37**	**2.28**	(9)
4110.79	20	$3d\,^4D_{1/2}-3p\,^4P_{3/2}$	0.0542:					0.0353:					0.0202:					(11)
4119.22	20	$3d\,^4D_{7/2}-3p\,^4P_{5/2}$	**0.178**	*	**2.06**	**2.01**	**1.08**	**0.133**	*	**1.54**	**1.50**	**0.80**	**0.197**	*	**2.28**	**2.23**	**1.19**	
4120.28	20	$3d\,^4D_{5/2}-3p\,^4P_{5/2}$	0.264					0.227					0.278					(12)
4369.28	26	$3d\,^2D_{3/2}-3p\,^2D_{3/2}$	0.0291					0.0383										(13)

Table 6. (b) Optical O II recombination lines in NGC 7009 (4f–3d transitions).

Wavelength (Å)	MT	Transition	Slit PA=0° CCD Spectra Intensity (Hβ=100)		O^{2+}/H^+ (10^{-3})	Slit PA=45° IPCS Spectra Intensity (Hβ=100)		O^{2+}/H^+ (10^{-3})	Slit PA=45° CCD Spectra Intensity (Hβ=100)		O^{2+}/H^+ (10^{-3})	Note
4107.33	47	4f D[3]$_{7/2}$–3d ^{4}F$_{5/2}$	0.0621:			0.0742:						(14)
4087.15	48	4f G[3]$_{5/2}$–3d ^{4}F$_{3/2}$	0.0629	*	2.12	0.0660	*	2.22	0.0533:	*	1.79	
4089.28	48	4f G[5]$_{11/2}$–3d ^{4}F$_{9/2}$	0.254	*	2.31	0.223	*	2.03	0.253	*	2.30	
4083.90	49	4f G[4]$_{7/2}$–3d ^{4}F$_{5/2}$	0.0692:		2.21	0.0495:		1.58	0.0776:		2.48	
4041.29	50	4f F[2]$_{5/2}$–3d ^{4}F$_{5/2}$	0.0561			0.0477			0.0935:			(15)
4035.07	51	4f F[3]$_{5/2}$–3d ^{4}F$_{5/2}$	0.0243:		8.10	0.0221:		7.37				(16)
4307.24	53	4f D[2]$_{3/2}$–3d ^{4}P$_{1/2}$				0.0203	*	1.76				
4317.70	53	4f D[3]$_{5/2}$–3d ^{4}P$_{3/2}$				0.0148:		1.89				
4288.82	54	4f D[1]$_{1/2}$–3d ^{4}P$_{1/2}$	0.0161	*	1.47	0.0347	*	3.16				(17)
4294.79	54	4f D[2]$_{5/2}$–3d ^{4}P$_{3/2}$	0.0593	*	1.89	0.0742	*	2.36	0.0814:	*	2.59	(18)
4303.84	54	4f D[3]$_{7/2}$–3d ^{4}P$_{5/2}$	0.127	*	2.39	0.133	*	2.50				(19)
4291.26	55	4f G[3]$_{7/2}$–3d ^{4}P$_{5/2}$	0.0409	*	1.46	0.0652	*	2.33				(20)
4315.39	64	4f D[1]$_{3/2}$–3d ^{4}D$_{3/2}$				0.0278:		2.27				(21)
4357.26	64	4f D[3]$_{7/2}$–3d ^{4}D$_{5/2}$	0.0135:		1.65	0.0214:		2.61				(22)
4332.71	65	4f G[4]$_{9/2}$–3d ^{4}D$_{7/2}$				0.0420		4.01				(23)
4275.56	67	4f F[4]$_{9/2}$–3d ^{4}D$_{7/2}$	0.237	*	1.69	0.248	*	1.77	0.256	*	1.83	(24)
4282.95	67	4f F[2]$_{5/2}$–3d ^{4}D$_{3/2}$	0.0862	*	2.65	0.0798	*	2.45	0.0578:		1.77	(25)
4353.59	76	4f G[3]$_{7/2}$–3d ^{2}F$_{5/2}$	0.0148:		1.28	0.0205:		1.78	0.0202:		1.75	(26)
4371.62	76	4f G[4]$_{9/2}$–3d ^{2}F$_{7/2}$	0.0200	*	1.84	0.0311	*	2.86				(27)
4285.69	78	4f F[3]$_{7/2}$–3d ^{2}F$_{5/2}$	0.0414	*	1.98	0.0521	*	2.49				(28)
4313.44	78	4f F[4]$_{9/2}$–3d ^{2}F$_{7/2}$	0.0169		1.27	0.0350		2.63				(29)
4446.81	86	4f D[1]$_{3/2}$–3d ^{2}P$_{3/2}$				0.0120:		7.49				(30)
4466.44	86	4f D[2]$_{5/2}$–3d ^{2}P$_{3/2}$	0.0431:		3.85	0.0329:		2.94				(31)
4489.46	86	4f D[2]$_{3/2}$–3d ^{2}P$_{1/2}$	0.0296:		4.11	0.0126:		1.75				
4491.23	86	4f D[3]$_{5/2}$–3d ^{2}P$_{3/2}$	0.0490	*	3.25	0.0480	*	3.18	0.0344:		2.28	
4477.90	88	4f G[3]$_{5/2}$–3d ^{2}P$_{3/2}$	0.0100:	*	1.06	0.0316	*	3.34				
4609.44	93	4f F[4]$_{7/2}$–3d ^{2}D$_{5/2}$	0.135	*	2.22	0.135	*	2.17	0.118	*	1.90	(32)
4621.27	92	4f F[2]$_{5/2}$–3d ^{2}D$_{5/2}$				0.0217:		10.4				(33)
4602.13	93	4f F[3]$_{5/2}$–3d ^{2}D$_{3/2}$	0.0298			0.0402			0.0522			(34)
4613.68	93	4f F[3]$_{7/2}$–3d ^{2}D$_{5/2}$	0.0193:		2.26	0.0220:		2.58				(35)
Sum			**1.14**		**2.06**	**1.24**		**2.19**	**0.762**		**2.04**	(36)
Average					2.18 ± 0.12			2.26 ± 0.08			2.08 ± 0.16	(37)

(1) Probably overestimated due to the influence of the much stronger N III λ4640.64 line nearby.
(2) Blending with N III λ4641.90 (M 2). The intensities listed are for O II λ4641.82 only. See text for details.
(3) Total intensity of the multiplet. See text for more details.
(4) Affected by the strong Hγ line nearby.
(5) Broad feature, probably blending with O II λ4366.530 and/or Ne II λ4365.72 (M 57).
(6) Also 3d ^{4}F$_{3/2}$–3p ^{4}D$_{1/2}$ λ4068.60 and weak C III lines of M 16, 5 ^{3}G–4 ^{3}F°. For NGC 7009, the three C III lines are not incorporated in the profile fitting. See text for details.
(7) Blending with [S II] λ4076.35.
(8) Measurement affected by the much stronger N III λ4097.31 line nearby.
(9) The total intensity listed here is the sum of those lines marked with an asterisk.
(10) Also 3d ^{4}D$_{5/2}$–3p ^{4}D$_{7/2}$ λ3883.13. Contribution from O II 3d ^{4}P–3p ^{4}D° λ3882.45 (M 11) should be negligible.
(11) There is possible contamination from O II λ4110.198 (^{1}D)3d ^{2}D$_{5/2}$–(^{1}D)3p ^{2}F°$_{5/2}$ (M 37). However, the other line (^{1}D)3d ^{2}D$_{5/2}$–(^{1}D)3p ^{2}F°$_{7/2}$ of the same multiplet at 4113.835 Å is not detected.
(12) Also 3d ^{4}D$_{3/2}$–3p ^{4}P$_{5/2}$ λ4120.54. Blending with He I λ4120.81 (M 16).
(13) Identification questionable. See text for details.
(14) Lies in the red wing of Hδ and N III λ4103.37. Intensity probably overestimated.
(15) Also 4f F[2]$_{3/2}$–3d ^{4}F$_{5/2}$ λ4041.95. Blending with N II λ4041.32 (M 39).
(16) Also 4f F[3]$_{7/2}$–3d ^{4}F$_{5/2}$ λ4035.46.
(17) Also 4f D[1]$_{3/2}$–3d ^{4}P$_{1/2}$ λ4288.82.
(18) Also 4f D[2]$_{3/2}$–3d ^{4}P$_{3/2}$ λ494.93.
(19) Also 4f D[3]$_{5/2}$–3d ^{4}P$_{5/2}$ λ4304.08 and 4f G[5]$_{9/2}$–3d ^{4}D$_{7/2}$ λ4303.62 (M 65). This feature is affected by cosmic ray on the PA=45° CCD spectra.
(20) Also 4f G[3]$_{5/2}$–3d ^{4}P$_{5/2}$ λ4291.86, 4f F[2]$_{3/2}$–3d ^{2}F$_{5/2}$ λ4292.98 and 4f F[2]$_{5/2}$ – 3d ^{2}F$_{5/2}$ λ4292.22. Broad feature.
(21) Also 4f D[1]$_{1/2}$–3d ^{4}D$_{3/2}$ λ4315.33, 4f D[19$_{3/2}$–3d ^{4}D$_{5/2}$ λ4315.68, 4f F[3]$_{5/2}$–3d ^{2}F$_{7/2}$ λ4315.352 and 4f F[3]$_{7/2}$–3d ^{2}F$_{7/2}$ λ4315.827.
(22) Also 4f D[3]$_{5/2}$–3d ^{4}D$_{5/2}$ λ4357.52, 4f D[3]$_{5/2}$–3d ^{4}D$_{7/2}$ λ4358.71, 4f D[3]$_{5/2}$–3d D$_{3/2}$ λ4357.22 and 4f D[3]$_{7/2}$–3d ^{4}D$_{7/2}$ λ4358.44.
(23) Lies at the blue wing of Hγ, intensity probably overestimated.
(24) Also 4f F[4]$_{7/2}$–3d ^{4}D$_{5/2}$ λ4273.10 4f F[4]$_{7/2}$–3d ^{4}D$_{7/2}$ λ4274.24, 4f F[3]$_{5/2}$–3d ^{4}D$_{3/2}$ λ4275.99, 4f F[3]$_{5/2}$–3d ^{4}D$_{5/2}$ λ4276.28, 4f F[3]$_{7/2}$–3d ^{4}D$_{5/2}$ λ4276.75, 4f F[3]$_{5/2}$–3d ^{4}D$_{7/2}$ λ4277.44, 4f F[2]$_{3/2}$–3d ^{4}D$_{1/2}$ λ4277.44, 4f F[2]$_{7/2}$–3d ^{4}D$_{7/2}$ λ4277.90, 4f D[1]$_{1/2}$–3d ^{4}P$_{3/2}$ λ4276.56 and 4f D[1]$_{3/2}$–3d ^{4}P$_{3/2}$ λ4276.61.
(25) Also 4f F[2]$_{5/2}$–3d ^{4}D$_{5/2}$ λ4283.25, 4f F[2]$_{3/2}$–3d ^{4}D$_{3/2}$ λ4283.73, 4f F[2]$_{3/2}$–3d ^{4}D$_{5/2}$ λ4284.00 and 4f F[2]$_{5/2}$–3d ^{4}D$_{7/2}$ λ4284.39.
(26) Also 4f G[3]$_{5/2}$–3d ^{2}F$_{5/2}$ λ4354.18.
(27) Also 4f G[4]$_{7/2}$–3d ^{2}F$_{7/2}$ λ4371.25.

(28) Also 4f F[3]$_{5/2}$–3d ^{2}F$_{5/2}$ λ4285.216.
(29) Poor wavelength agreement. λ_{obs} = 4314.10 ± 0.35 Å. An alternative identification as C II λ4313.50 suffers from a similar discrepancy.
(30) Also 4f D[1]$_{1/2}$–3d ^{2}P$_{3/2}$ λ4446.81.
(31) Also 4f D[2]$_{3/2}$–3d ^{2}P$_{3/2}$ λ4466.59.
(32) Also 4f F[2]$_{5/2}$–3d ^{2}D$_{3/2}$ λ4610.20.
(33) Also N II λ4621.39 (M 5).
(34) Also N II λ4601.48 (M 5).
(35) Also 4f F[3]$_{5/2}$–3d ^{2}D$_{5/2}$ λ4613.14, N II λ4613.87 (M 5).
(36) The total intensity is the sum of those 4f–3d lines marked with an asterisk.
(37) Average and 1 σ standard error of abundances derived from those 4f–3d lines marked with asterisks, having intensities larger than 0.05 in units of Hβ = 100, with equal weight.

Table 7. Optical O II recombination lines in NGC 7009 with parentage other than ^{3}P.

Wavelength (Å)	MT	Transition	Intensity (Hβ=100) PA=0° CCD	PA=45° IPCS	PA=45° CCD	Note
4590.97	15	(^{1}D)4p ^{2}F$_{7/2}$–(^{1}D)3s ^{2}D$_{5/2}$	0.0907	0.0754	0.0752	
4596.18	15	(^{1}D)4p ^{2}F$_{5/2}$–(^{1}D)3s ^{2}D$_{3/2}$	0.0424	0.0476	0.0476	(1)
4347.42	16	(^{1}D)3p ^{2}D$_{3/2}$–(^{1}D)3s ^{2}D$_{3/2}$		0.0700:		(2)
4351.26	16	(^{1}D)3p ^{2}D$_{5/2}$–(^{1}D)3s ^{2}D$_{5/2}$		0.0277:		
4448.19	35	(^{1}D)3d ^{2}F$_{7/2}$–(^{1}D)3p ^{2}F$_{7/2}$		0.0130:		(3)
4185.45	36	(^{1}D)3d ^{2}G$_{7/2}$–(^{1}D)3p ^{2}F$_{5/2}$	0.0572	0.0450	0.0580:	
4189.79	36	(^{1}D)3d ^{2}G$_{9/2}$–(^{1}D)3p ^{2}F$_{7/2}$	0.0703	0.0501	0.0747	
4467.92	94	(^{5}S)3p ^{6}P$_{5/2}$–(^{5}S)3s ^{6}S$_{5/2}$	0.0431:	0.0510:	0.0510:	(4)
4254.13	101	(^{1}D)4f H[5]$_{9/2}$–(^{1}D)3d ^{2}G$_{7/2}$	0.0318:	0.0261:	0.0249:	(5)
4487.72	104	4f D[2]$_{3/2}$–(^{1}D)3d ^{2}P$_{1/2}$		0.0087:		
4488.20	104	4f D[2]$_{3/2}$–(^{1}D)3d ^{2}P$_{3/2}$		0.0168:		(6)

(1) Also (^{1}D)4p ^{2}F$_{5/2}$–(^{1}D)3s ^{2}D$_{5/2}$ λ4595.96.
(2) Also (^{1}D)3p ^{2}D$_{3/2}$–(^{1}D)3s ^{2}D$_{5/2}$ λ4347.22. Probably overestimated due to the poorly defined continuum level near the strongly saturated Hγ.
(3) Also (^{1}D)3d ^{2}F$_{5/2}$–(^{1}D)3p ^{2}F$_{7/2}$ λ4447.67.
(4) Also (^{5}S)3p ^{6}P$_{7/2}$–(^{5}S)3s ^{6}S$_{5/2}$ λ4465.42. Probably overestimated due to the influence of the much stronger He I λ4471.48 line nearby.
(5) Also (^{1}D)4f H[5]$_{11/2}$–(^{1}D)3d ^{2}G$_{9/2}$ λ4253.90.
(6) Also 4f D[2]$_{5/2}$–(^{1}D)3d ^{2}P$_{3/2}$ λ4488.20.

note, however, that all of these lines are extremely weak, indicating that the effects of dielectronic recombination on highly excited levels of O II are small, in agreement with the theoretical calculations of Nussbaumer & Storey (1984).

5.1.1 *Multiplet 1, 3p ^{4}D°–3s ^{4}P*

This multiplet is the strongest as well as the best observed. A spectrum showing the relevant wavelength region is presented in Fig. 1. In addition to lines from O II M 1, we find in this region lines from N III M 2 excited by the Bowen fluorescence mechanism, lines from C III M 1, one weak permitted line of N II (M 5), and a blended feature due to C IV and [Fe III]. The O II λ4638.86 line is partially resolved from N III λ4640.64. However, accurate measurements of this line are difficult due to the strength of the N III line, which is about 10 times stronger. Another O II line of this multiplet, λ4641.82, coincides in wavelength with N III λ4641.81. These three features, together with N III λ4634.16 and N II λ4630.56, were fitted by five Gaussian profiles, assuming all the five components to have the same FWHM and that the difference between the observed wavelengths of O II λ4638.86 and N III λ4640.64 was the same as the difference between their laboratory wavelengths. The resultant fit is also plotted in Fig. 1. An estimate of the contribution of N III λ4641.81 to the blend at λ4642 can be obtained by considering the fact that N III $\lambda\lambda$4634.16 and 4641.81 decay from the same upper level, so that their intensity ratio depends only on the coupling scheme but not on the excitation mechanism. Under LS-coupling, $I(\lambda 4641.81) = 0.2I(\lambda 4634.16)$. The intensities of O II λ4641.82 estimated in this way are listed in Table 5. N III λ4641.81 contributes about 35 per cent of the total intensity of the blend.

Two other lines of O II M 1, $\lambda\lambda$4649.14 and 4650.84, blend with three lines of C III 3p ^{3}P°–3s ^{3}S (M 1), $\lambda\lambda$4647.40, 4650.16 and 4651.35. This complex was fitted using five Gaussian profiles of the same FWHM, utilizing their known relative wavelengths. In addition, the intensity ratios of the three C III components were assumed to be as in LS-coupling, i.e. 5:3:1. The relative intensities of the two O II lines were, however, not constrained. The remaining three lines from O II M 1 observed, $\lambda\lambda$4661.63, 4673.74 and 4676.24, are free of blending effects. The Gaussian line profile fits to these lines are also plotted in Fig. 1. As an example, the formal

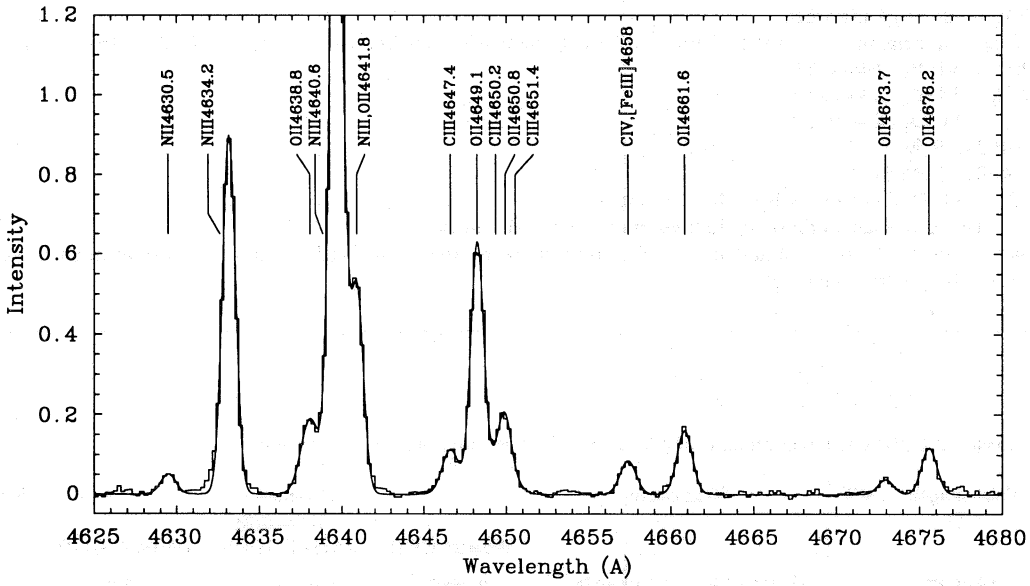

Figure 1. IPCS spectrum of NGC 7009 obtained at the AAT, showing the O II M 1 lines. The continuous line overplotted is the sum of a multiple Gaussian fit to the lines. Interstellar reddening has been corrected for, and the intensity is normalized such that $I(\mathrm{H}\beta)=100$. See text for more details.

errors in the intensities of $\lambda\lambda$4638.86, 4649.14, 4661.63 and 4673.74 estimated from the ELF line-fitting procedure in DIPSO (Howarth & Murray 1988) were, respectively, 30, 5, 12 and 33 per cent.

Except for the weakest line at λ4696.35, all O II lines of this multiplet have been observed in the spectrum of NGC 7009. Thus it is possible to compare their relative intensities with those expected in LS-coupling – the results are shown in Table 8. Columns 1–3 list the lines being compared, the J values of the lower and upper levels of the transitions, and the predicted intensities in LS-coupling, in units of $I_{\mathrm{LS}}(\lambda 4649.14)=1.0$. The last three columns give the ratios of the observed and predicted intensities, as measured for NGC 7009 from the PA = 45° IPCS spectra, the PA = 45° CCD spectra, and the PA = 0° CCD spectra, respectively. Again the ratios are scaled to unity for λ4649.14. Table 8 shows that there is quite good agreement between the observations and the predictions of LS-coupling, except for λ4638.86 where the intensities measured on the IPCS spectra are about a factor of 2 higher than predicted. The discrepancy increases to a factor of 3 on the CCD spectra, which have slightly lower resolution. As mentioned above, the accurate measurement of this line is frustrated by its blending with a much stronger line. There is marginal evidence that the weak λ4673.74 line is also stronger than expected. This line coincides in wavelength with C III λ4673.91 (M 5). However, a significant contribution from the C III line seems unlikely, as judged from the absence of C III λ4665.90 of the same multiplet, which is expected to be three times stronger than the λ4673.91 line.

5.1.2 *Multiplet 2, $3p\,^4P^\circ$–$3s\,^4P$*

Even at a resolution of 1 Å, the accurate measurement of the two strongest components of this multiplet, $\lambda\lambda$4345.56 and 4366.89, is hindered by the presence of the strong Hγ and [O III] λ4363 transitions. However, the component at 4349.43 Å is well measured. There is an indication that λ4317.14 is too strong as compared to λ4319.63. Under LS-coupling, they should have an intensity ratio of 0.926, compared to the observed value of 1.4 measured on the IPCS spectrum (Table 6a). The λ4317.14 line is blended with one of the 3d–4f transitions at λ4317.70 and Gaussian line profile fitting was used to retrieve their intensities, utilizing the known relative wavelengths. The derived intensity of λ4317.70 is consistent with its effective recombination coefficient presented in Section 4. On the IPCS spectrum, $\lambda\lambda$4349.43 and 4319.63 have an intensity ratio of 2.4, in good agreement with the LS-coupling value of 2.33.

Table 8. Comparison of the observed and predicted relative intensities of O II M 1 in NGC 7009.

Line	J–J′	I_{LS}	I_{obs}/I_{LS}		
4649.14	5/2–7/2	1.000	1.0	1.0	1.0
4641.82	3/2–5/2	0.525	1.6	1.2	1.3
4661.63	3/2–3/2	0.267	1.1	1.2	1.1
4676.24	5/2–5/2	0.225	1.0	1.1	1.2
4638.86	1/2–3/2	0.208	2.1	3.0	3.3
4650.84	1/2–1/2	0.208	1.2	1.2	1.4
4673.74	3/2–1/2	0.042	1.7	2.3	2.6
4696.35	5/2–3/2	0.025	–	–	–

5.1.3 *Multiplet 5, $3p\,^2D^\circ$–$3s\,^2P$*

This is the only doublet observed from the 3–3 group. The relative line intensities are in good agreement with the LS-coupling values (Table 5a).

5.1.4 *Multiplet 10, $3d\,^4F$–$3p\,^4D^\circ$*

Several major components of this strong multiplet are unfortunately seriously affected by line blending. A spectrum of

NGC 7009 in this wavelength region is shown in Fig. 2(a). The λλ4069.62 and 4069.89 lines are partially blended with [S II] λ4068.60, whereas λ4075.86 is blended with [S II] λ4076.35. Near 4070 Å, there are three lines from C III M 16 5g ^{3}G–4f ^{3}F°: λ4067.87 (J=3–2), λ4068.97 (J=4–3) and λ4070.30 (J=5–4), with intensity ratios of 1.00:1.31:1.71 under pure LS-coupling. In contrast to C III M 1 at 4650 Å, which is mainly excited by dielectronic recombination, C III M 16 is primarily excited by radiative recombination. From the effective radiative and dielectronic recombination coefficients given by Péquignot et al. (1991) and Nussbaumer & Storey (1984) respectively, we have C III I(M 16)/I(M 1)=0.56. In the case of NGC 7009, emission from [S II] and O II dominates the blend at 4070 Å, so the three C III lines have not been incorporated in the fitting. In contrast, in objects of higher excitation class, the blend may be dominated by emission from C III M 16. As an example, a spectrum of NGC 3242 showing the same wavelength region is plotted in Fig. 2(b). The spectrum was secured during the 1993 observing run at ESO with the 1.5-m telescope (Barlow et al. 1995, in preparation). In this case, the blend was fitted by including contributions from the [S II], O II and C III lines. When fitting the NGC 3242 spectrum, the relative intensities of the three C III lines were constrained to their LS-coupling values, and similarly for the two O II lines. The derived total intensities of C III M 1 and M 16 give I(M 16)/I(M 1)=1.1, about a factor of 2 higher than the theoretical value of 0.56.

The intermediate coupling calculations in Section 4 show that there is no significant departure from pure LS-coupling for the ^{4}F term. However, the spectra shown in Fig. 2 indicate that λ4072.16 is stronger than expected. For example, λλ4072.16 and 4075.86 have an intensity ratio of 0.685 under pure LS-coupling, whereas our intermediate coupling calculations predict 0.692. The discrepancy can be best seen in Fig. 2(b), where the λ4072.16 line is actually observed to be stronger than the total intensity of the blend of [S II] λ4076.35 and O II λ4075.86. The contribution of the [S II] λ4076.35 line to the blend at 4076 Å can be estimated from the observed intensity of [S II] λ4068.6. Calculations of level populations of [S II] using a five-level atomic model show that the intensity ratio of [S II] λ4068.6 to λ4076.35 has a value of 3.04 which is nearly independent of the temperature and density for $N_e < 5\times10^4$ cm^{-3}. For NGC 3242, after the contribution from the [S II] line to the 4076-Å blend (about 8.6 per cent) has been subtracted, we have O II I(λ4072.16)/I(λ4075.86)=1.47. Using the IPCS data, similar calculations for NGC 7009 (where the correction amounts to 38 per cent) give I(λ4072.16)/I(λ4075.86)=1.24. In both cases the observed ratio is about a factor 2 higher than that expected from LS-coupling. A likely explanation for this discrepancy is that λ4072.16 is contaminated by some unknown line, although we failed to find any convincing candidate. NGC 3242 is unique among the objects we have observed in the sense that it has very weak [S II] emission. Further observations of objects showing weak [S II] emission may help to clarify the ambiguity. The intensities of other lines of O II M 10, λλ4078.84, 4085.11 and 4092.93, relative to the corrected intensity of λ4075.86, agree well with the predictions of LS-coupling.

5.1.5 *Multiplet 12, 3d ^{4}D–3p ^{4}D°*

Only one line of this multiplet has been observed, which is a blend of λ3882.19 (J=7/2–7/2) and λ3883.13 (J=5/2–7/2). Aller & Kaler (1964) attributed this line to O II 3d ^{4}P–3p ^{4}D° λ3882.45 (M 11). However, from the effective recombination coefficients predicted for these two multiplets, the contribution of M 11 should be completely negligible.

5.1.6 *Multiplet 19, 3d ^{4}P–3p ^{4}P°*

The calculations presented in Section 4 show that the wave functions of the levels of the upper term of this multiplet are

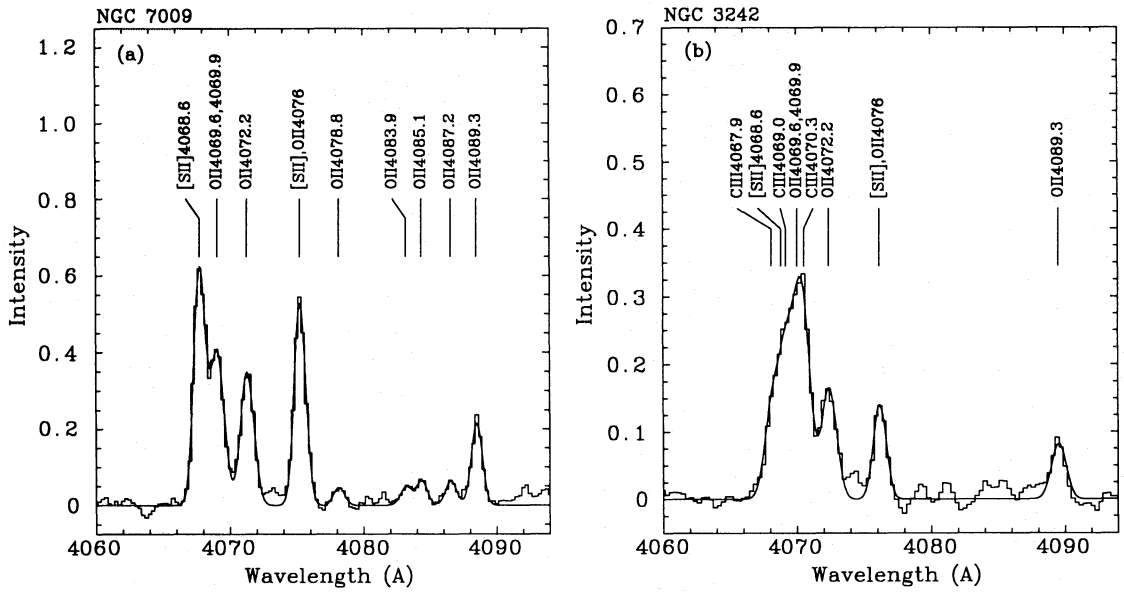

Figure 2. Spectra of (a) NGC 7009 and (b) NGC 3242 between 4060 and 4094 Å. The three O II lines at λλ4083.90, 4087.15 and 4089.28 are from 3d–4f transitions; the remaining O II lines belong to M 10. The continuous line is a multiple Gaussian fit to the observed lines. See also the caption to Fig. 1 and text for more details.

mixed with those of 3d ^{4}D and 3d ^{2}F. Although this multiplet is weak, three of its lines, at $\lambda\lambda$4153.30, 4156.53 and 4169.22, are well detected in the spectrum of NGC 7009 and show abnormal intensity ratios, 1:0.75:0.65, as compared to 1:1:2.33 predicted under LS-coupling and 1:0.16:0.340 under intermediate coupling. Thus the agreement between the observations and theoretical predictions are poor in both cases. There is one line from C III at 4156.49 Å (M 21); however, the expected stronger C III λ4162.86 line of the same multiplet is not detected. The radiative recombination coefficient of C III M 21 is not listed in Péquignot et al. (1991), but is presumably smaller than that of λ4187.05 (M 18). The dielectronic recombination coefficients of both multiplets are available from Nussbaumer & Storey (1984), with that of M 21 being 30 per cent lower than that of M 18. The λ4187.05 line has been detected on the IPCS spectrum and has an intensity of 0.05. Thus, unless all the energy of C III M 21 goes to the λ4156.49 line (only 30 per cent should go under LS-coupling), contamination from this line of the observed intensity of O II λ4156.53 is not enough to explain the discrepancy. No plausible lines which might be blending with O II λ4153.30 were found.

5.1.7 *Multiplet 20, 3d ^{4}D–3p ^{4}P°*

Only one line of this multiplet, λ4119.22, is observed, partially blended with He I λ4120.81.

5.1.8 *Multiplet 26, 3d ^{4}D–3p ^{4}D°*

Aller & Kaler (1964) attributed a feature near 4369 Å to the O II λ4369.28 line. The identification is, however, questionable. First, the expected stronger component of this multiplet, λ4395.94, is missing. Secondly, as measured on our spectra, this feature has a laboratory wavelength of 4369.78 ± 0.15 Å, which is only in fair agreement with the predicted wavelength of O II λ4369.28. A more plausible identification is Ne II λ4369.77 (M 56).

5.1.9 *4f–3d transitions*

About 30 measurements of transitions from this group were obtained for NGC 7009. As mentioned before, LS-coupling breaks down for these transitions. However, the effective recombination coefficient of λ4089.28, the strongest transition of this group, is not dependent on the coupling scheme in which the calculations are made. Spectra showing this line in NGC 7009 and 3242 are illustrated in Fig. 2. The effective recombination coefficients of the 4f–3d lines are almost independent of optical depth and are more reliable than those of the 3–3 transitions, which make them best for the purpose of abundance determination. However, most of these lines are quite weak and are much more difficult to observe.

The breakdown of LS-coupling for the 4f–3d transitions is clearly shown by the appearance of some lines that are forbidden in LS-coupling. In Table 9, we compare the observed intensities of some 4f–3d lines with their predicted values in LS-coupling and in intermediate coupling. The observed data are taken from the PA = 45° IPCS spectra, and all lines marked by asterisks in Table 6 are included. Consecutive columns give the wavelength of the line, the dereddened intensity and the intensities predicted by LS-coupling and intermediate coupling, respectively. The intensities are normalized to $I(\lambda 4089.28) = 1.00$. Some of the lines listed here are actually blends of several components, and a listing of components other than the one listed in the table can be found in the footnotes to Table 6. Obviously, LS-coupling fails completely to predict the lines at $\lambda\lambda$4087.15, 4303.84, 4371.62, 4285.69 and 4491.23. The effect of the breakdown of LS-coupling is to reallocate the energy available among more transitions than are allowed by pure LS-coupling. The results are the appearance of some new lines at the expense of the weakening of some lines that are strong in LS-coupling. Such a trend is clearly visible in Table 9. The close agreement between the observations and the theoretical calculations for intermediate coupling demonstrates the validity and accuracy of the effective recombination coefficients presented in Section 4.

5.2 O^{2+} abundance determination

Let $I(\lambda)$ be the intensity of one of the observed O II recombination lines at wavelength λ; then the ionic abundance O^{2+}/H^+ is given by

$$\frac{O^{2+}}{H^+} = \frac{\lambda(\text{Å})}{4861}\frac{\alpha_{\text{eff}}(H\beta)}{\alpha_{\text{eff}}(\lambda)}\frac{I(\lambda)}{I(H\beta)}, \quad (4)$$

where α_{eff} represents the effective recombination coefficient. For $\alpha_{\text{eff}}(H\beta)$, we use the analytic fit given by Péquignot et al. (1991) for case B. For the 3p–3s transitions, $\alpha_{\text{eff}}(\lambda)$ is taken from Storey (1994), assuming that the relative intensities of lines within a multiplet follow those predicted in LS-coupling. For the 3d–3p and 4f–3d transitions, we use the new calculations made in intermediate coupling presented in Section 4, with $\alpha_{\text{eff}}(\lambda)$ for individual lines given by equations (1) and (3). The O^{2+}/H^+ abundance given by the above equation is essentially independent of electron density for $N_e < 10^6$ cm^{-3}, and only weakly dependent on electron temperature; it changes less than 10 per cent as T_e varies from 8000 to 12 000 K. For NGC 7009, all the ionic abundances of O^{2+} derived from optical recombination lines, as well as

Table 9. Comparison of the observed and the predicted intensities of O II 4f–3d transitions in NGC 7009.

Line	I_{obs}	I_{LS}	I_{IC}
4087.15	0.30	0.00	0.27
4089.28	1.00	1.00	1.00
4307.24	0.09	0.11	0.10
4288.82	0.16	0.11	0.10
4294.79	0.33	0.42	0.29
4303.84	0.60	0.00	0.48
4291.26	0.29	0.54	0.26
4275.56	1.11	1.49	1.27
4282.95	0.36	0.51	0.30
4371.62	0.14	0.00	0.10
4285.69	0.23	0.06	0.19
4491.23	0.22	0.00	0.14
4477.90	0.14	0.32	0.09
4609.44	0.60	0.52	0.57

those of C and N described in the next section, are calculated assuming $T_e = 10\,000$ K.

The O^{2+} abundances thus derived from equation (4) are listed in Table 6. The letters A, B and C refer to the cases defined in Section 4. The emissivity of the 4f–3d transitions is insensitive to the optical depth and thus independent of the case assumed. Lines used for abundance determination are marked with an asterisk in Table 6. Abundances from individual lines as well as from the total intensities of the multiplets are given, except for those lines seriously affected by line blending. For the 3p–3s transitions, the total intensity of a multiplet is calculated by adding the lines marked with asterisks. The contribution from unobserved lines or those seriously affected by blending are taken into account assuming that LS-coupling applies. For the 3d–3p and 4f–3d transitions, the total intensities (labelled as 'Sum' in Table 6) are the simple sum of the intensities of the lines marked with asterisks. The average and 1σ standard error of the abundances derived from the 4f–3d lines that are marked with asterisks, *and* that have intensities larger than 0.05, are listed at the end of Table 6(b). Since the intensities of stronger lines tend to be better measured simply due to higher S/N ratios, abundances deduced from the total intensity of each multiplet are preferred over those from the individual components. In addition to the 4f–3d transitions, the abundances deduced from M 1, 10, 12 and 20 are nearly independent of the case assumed. For those more sensitive to the case assumed, from inspection of Table 6(a) it seems that case B is more appropriate for quartets and case A for doublets, where M 5 is the only doublet observed among the 3–3 transitions. This is consistent with the results of Peimbert et al. (1993).

Fig. 3 shows the abundances derived from different multiplets and from the 4f–3d group of transitions. The significant improvement in the degree of consistency between abundances deduced from different multiplets when using recombination coefficients calculated in intermediate coupling, rather than LS-coupling, is apparent. For the three 3p–3s multiplets, no calculations of their effective recombination coefficients under intermediate coupling have been done – two of them give systematically lower abundances using effective recombination coefficients in LS-coupling. A plausible explanation is that the cascading to the 3p terms is reduced by the effects of intermediate coupling, particularly in the nd–3p transitions. The breakdown of LS-coupling among (^3P)nd states can result in decays directly to the ground electron configuration, which are not permitted in LS-coupling, and which bypass the (^3P)3p terms. Thus even though the 3p terms are calculated by treating the whole ion in LS-coupling, the rate coefficients calculated by treating the whole ion in LS-coupling may have actually been overestimated, thereby giving abundances that are too low. However, as discussed in Section 4, a fully self-consistent calculation, treating the whole ion in intermediate coupling and solving the resultant collisional-radiative recombination problem, is not feasible at the moment. Note that in Fig. 3 the abundances deduced from the 4f–3d transitions using LS-coupling recombination coefficients are very close to those derived using the intermediate coupling coefficients. This apparent agreement simply reflects the fact that the abundances plotted in Fig. 3 were derived by summing the intensities of all useful lines observed. We have shown in Section 4 that LS-coupling fails completely in describing individual 4f–3d transitions. In Fig. 4, we show the abundances deduced from individual 4f–3d lines. The failure of LS-coupling is obvious.

In Table 10, we present the O^{2+} abundances derived using the effective recombination coefficients of Péquignot et al. (1991), and compare them to those derived from the recombination coefficients presented here. Péquignot et al. (1991) did not list an effective recombination coefficient for M 5, and for M 12, M 19 and M 20 only results for case A were given. According to the calculations of Storey (1994), the effective recombination coefficients of M 12 and M 20 change by less than 3 per cent from case A to case B. However, for M 19 the coefficient increases by a factor of 26

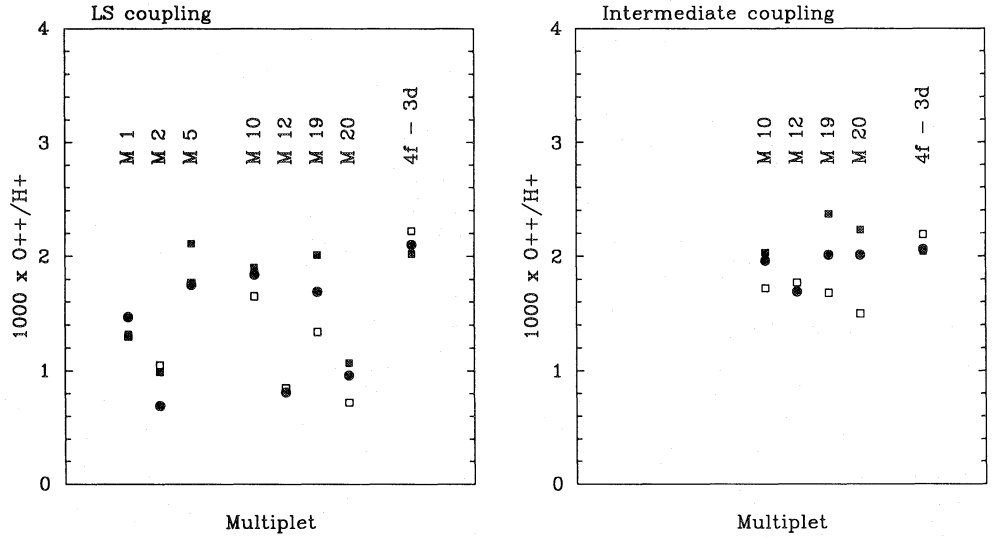

Figure 3. O^{2+}/H^+ abundances for NGC 7009 derived from different multiplets or groups of lines, using effective recombination coefficients based on LS-coupling and on intermediate coupling. For the M 5 doublet, results assuming case A have been used; for the remaining multiplets and for the 4f–3d transitions, case B has been assumed. Filled circles: PA = 0° CCD data; open boxes: PA = 45° IPCS data; filled boxes: PA = 45° CCD data.

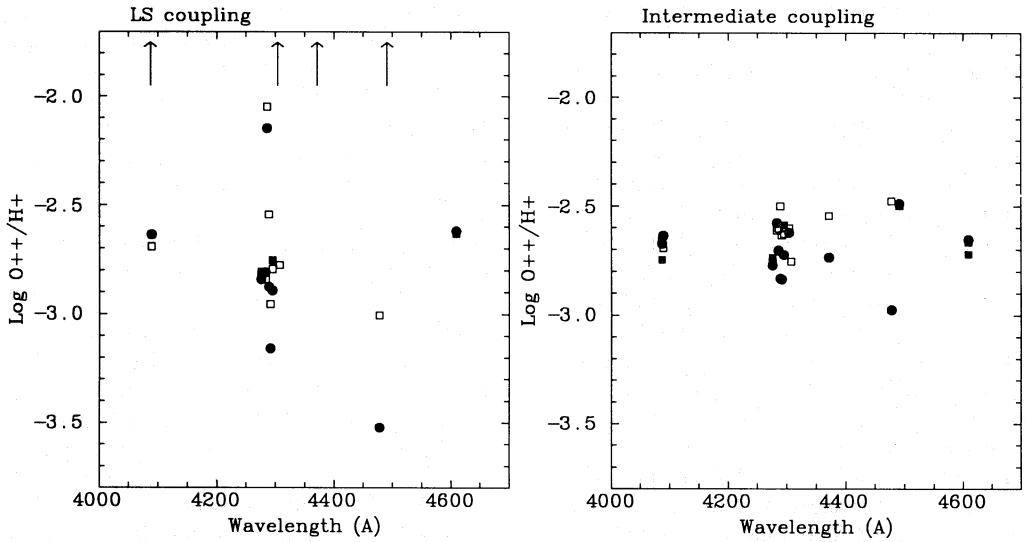

Figure 4. O^{2+}/H^+ abundances for NGC 7009 derived from individual lines of the 4f–3d group using effective recombination coefficients based on LS-coupling and on intermediate coupling. All transitions marked by an asterisk in Table 6(b) are shown. The four lines at $\lambda\lambda$4087.15, 4303.84, 4371.62 and 4491.23 are forbidden under LS-coupling and thus give infinite abundances. They are indicated by arrows. The observed intensities of the lines plotted span a range from 0.01 to 0.25, in units of $H\beta = 100$. The different symbols have the same meaning as in Fig. 3.

Table 10. Comparison of O^{2+} abundances for NGC 7009 derived from O II recombination lines using $\alpha_{\rm eff}(\lambda)$s from this work and from Péquignot et al. (1991, PPB).

Multiplet	PA=0° CCD Data $10^3\times O^{2+}/H^+$				PA=45° IPCS Data $10^3\times O^{2+}/H^+$			
	A		B		A		B	
	This work	PPB	This work	PPB	This work	PPB	This work	PPB
M 1	1.53	1.49	1.47	1.45	1.35	1.32	1.30	1.28
M 2	0.98	0.58	0.69	0.45	1.45	0.87	1.05	0.68
M 10	1.96	2.39	1.96	2.39	1.72	2.14	1.72	2.14
M 12	1.75	0.98	1.69		1.84	1.02	1.77	
M 19	44.8	2.09[a]	2.01		37.4	1.66[a]	1.68	
M 20	2.06	1.20	2.01		1.54	0.90	1.50	
λ4089.28	2.31	2.29	2.31		2.03	2.01	2.03	

[a]Case B?

Table 11. Comparison of O^{2+} abundances derived from recombination lines and from collisionally excited forbidden lines.

	PA=45°	PA=0°
	Recombination lines	
$10^4\times O^{2+}/H^+$	17.0 ± 1.0	17.6 ± 1.7
$10^4\times O/H$	18.8	19.6
	Forbidden lines	
$10^4\times O^+/H^+$	0.08	0.05
$10^4\times O^{2+}/H^+$	3.83	3.53
$10^4\times O/H$	4.22	3.94

from case A to case B. It seems to us that the effective recombination coefficient for M 19 given by Péquignot et al. for case A is actually for case B. Obviously, our current calculations give much more consistent results.

5.3 Oxygen abundances from recombination lines and from forbidden lines

Our final O^{2+} abundances derived from the O II recombination lines are given in Table 11. They are averages with results from the 3–3 multiplets and from the 4f–3d transitions given equal weight. The results listed in boldface in Table 6 were the ones used to obtain these averages, and the errors are 1σ standard errors. Except for the M 5 doublet, where case A has been adopted, case B has been assumed throughout. For PA=45°, the adopted value is an average of the results from the IPCS and CCD spectra, with weights of 2 and 1, respectively. [If we exclude the three multiplets from the 3p–3s transitions, i.e. M 1, M 2 and M 5 for which only LS-coupling recombination coefficients are available, then the average abundance ratio O^{2+}/H^+, from the four 3d–3p multiplets, as well as the 4f–3d transitions, are $(1.95\pm0.06)\times10^{-4}$ from PA=0° CCD data, $(1.77\pm0.11)\times10^{-4}$ from PA=45° IPCS data, and $(2.17\pm0.12)\times10^{-4}$ from PA=45° CCD data.] As well as the results from the recombination lines, the O^+ and O^{2+} abundances derived from the collisionally excited lines [O II] $\lambda\lambda$3726, 3729 and [O III] $\lambda\lambda$4959, 5007 are also listed in Table 11. They were calculated using the electron temperature derived from the [O III] nebular to auroral line ratio and the 'adopted' electron density, both listed in Table 2.

The total oxygen abundance relative to hydrogen is calculated from the ionic abundances of O^+ and O^{2+} using

$$\frac{O}{H}=\frac{O^+ + O^{2+}}{H^+}\times icf(O), \tag{5}$$

where $icf(O)$ is the empirical ionization correction factor given by

$$icf(O)=\left[\frac{He^+ + He^{2+}}{He^+}\right]^{2/3}. \tag{6}$$

The results are listed in Table 11. This formulation for *icf*(O) as well as that for *icf*(C) given below are based on photoionization modelling of a number of well-studied nebulae by one of us (RESC). The ionic abundances of He^+ and He^{2+} have been given in Table 2. O^+ abundances from recombination lines are not available, so in calculating O/H from the recombination lines, we have assumed that the O^+/O^{2+} ratio is the same as that deduced from the forbidden lines. By measuring three weak O III recombination lines near λ3265 that are not affected by charge exchange or Bowen fluorescence, Liu & Danziger (1993a) derived $O^{3+}/H^+ = 2.51\times10^{-4}$ in NGC 7009 from long-slit spectra secured with PA=0°. Adding this value to the O^{2+} abundance obtained from the O II recombination lines, listed in Table 11 for the same slit position, we find a total O/H abundance ratio in NGC 7009, based entirely on recombination line measurements, of 2.01×10^{-3} (the ionic concentrations of O^+ and of ionization stages higher than O^{3+} are both negligible in NGC 7009). This agrees within 3 per cent with that found by applying the *icf* correction to the ionic abundance of O^{2+} alone.

The most remarkable result in Table 11 is the extraordinarily high oxygen abundance in NGC 7009 found from recombination lines, about a factor of 5 higher than that derived from the forbidden lines. The close agreement between the results for two different slit positions, where the observations were taken using different telescopes as well as different kinds of detector, excludes the possibility that the discrepancy is due to observational errors. This unusual result is discussed further in Section 7.

6 THE C AND N ABUNDANCES DERIVED FROM RECOMBINATION LINES

As well as the numerous O II recombination lines, some important recombination lines from C and N ions were also observed in our spectra, including the well-known C II λ4267 line studied previously in NGC 7009 by Barker (1983). The relative intensities and the ionic abundances derived from these recombination lines are listed in Table 12.

C III M 1 λ4650 consists of three lines, close in wavelength, which blend with two lines of O II M 1. Their intensities were retrieved using multiple Gaussian profile fitting, as described in Section 5, and a spectrum showing this wavelength region has been illustrated in Fig. 1. The intensity of C III λ4650 listed in Table 12 is the total intensity of the three components. In addition to lines from C III M 1, C III λ4187 M 18 5g ^{1}G–4f ^{1}F° has also been observed. The C^{3+} abundance derived from this line is in good agreement with that from M 1. C IV λ4658.4 (M 6) is blended with [Fe III] λ4657.7. The intensities of this line for the two slit positions listed in Table 12 may contain a small contamination from the [Fe III] line. For PA=45°, the intensities of all the carbon lines listed in Table 12 agree within 10 per cent whether measured on the IPCS or on the CCD spectra, and are averaged with weights of 2 and 1, respectively, to give the tabulated values.

The N^{2+}/H^+ abundance ratio is derived from N II M 39 4f ^{3}G–3d ^{3}F° λ4042. The N II M 5 3p ^{3}P–3s ^{3}P° line observed at 4630 Å (Section 5.1 and Fig. 1) is not suitable for abundance determination, as it is seriously affected by optical depth effects: its effective recombination coefficient increases by a factor of 5.3 from case A to case B [Escalante & Victor 1990; for reference, the N^{2+}/H^+ ratios derived from N II M 5 are, for PA=0°, 3.72×10^{-3} (case A) and 7.09×10^{-4} (case B) and, for PA=45°, 2.51×10^{-3} (case A) and 4.78×10^{-4} (case B)]. Lines from M 39 are extremely weak, simply due to the small recombination coefficient. Only the two strongest components from this multiplet are detected, λ4041.32 (J=5–4) and λ4043.54 (J=4–3). N II λ4041.32 is blended with O II $\lambda\lambda$4041.27, 4041.95 from the 4f–3d group. Using the effective recombination coefficients given in Section 4, we predict $I(\lambda4041.27+\lambda4041.95) = 0.0239I(\lambda4089.28)$. Thus the contribution from the O II lines to the λ4041 blend can be estimated from the observed intensity of λ4089.28 listed in Table 6, and amounts to about 10 per cent. The relative intensities derived for N II λ4041.32 after this correction are listed in Table 12. It is worthwhile noting that N II λ4041.32 shares the merit of O II λ4089.28 in that its effective recombination coefficient is independent of the coupling scheme assumed. In calculating the N^{2+} abundance we have, however, utilized both the λ4041.32 and the λ4043.54 lines. To find the abundance of N^{3+}, we made use of N III M 17 5g ^{2}G–4f ^{2}F° λ4379. Owing to the high excitation energy of the upper level and the large angular momentum of the terms involved, this multiplet as well as N II M 39 are likely to be excited only by recombination.

Table 12. Carbon and nitrogen abundances derived from optical recombination lines in the spectrum of NGC 7009. The line intensities are in units of $I(H\beta)=100$.

	PA=45°	PA=0°
$I(\lambda4267)$	0.838	0.781
$10^4\times C^{2+}/H^+$	7.92	7.38
$I(\lambda4650)$	0.274	0.438
$10^4\times C^{3+}/H^+$	0.829	1.32
$I(\lambda4187)$	0.0533	0.102
$10^4\times C^{3+}/H^+$	0.787	1.51
$I(\lambda4658)$	0.106	0.081
$10^4\times C^{4+}/H^+$	0.239	0.182
$10^4\times C/H$	9.27	9.22
$I(\lambda4041)$	0.0424	0.0633
$I(\lambda4043)$	0.0361	0.0254
$10^4\times N^{2+}/H^+$	3.10	3.51
$I(\lambda4379)$	0.312	0.397
$10^4\times N^{3+}/H^+$	1.34	1.71
$10^4\times N/H$	4.71	5.54

All the abundances listed in Table 12 have been calculated using effective recombination coefficients from Péquignot et al. (1991) and dielectronic recombination coefficients from Nussbaumer & Storey (1984). They are insensitive to the assumption of case A or B. For N II M 39, the effective recombination coefficient given by Péquignot et al. (1991) is only 5 per cent lower than that of Escalante & Victor (1990) at $T_e = 10\,000$ K.

The total carbon abundance relative to hydrogen is calculated from the ionic abundances of C^{2+} and C^{3+}, using

$$\frac{C}{H} = \frac{C^{2+}+C^{3+}}{H^+}\times icf(C) \qquad (7)$$

and

$$icf(\mathrm{C}) = \left[\frac{\mathrm{He}^{+} + \mathrm{He}^{2+}}{\mathrm{He}^{+}}\right]^{1/3} \times \left[\frac{\mathrm{O}^{+} + \mathrm{O}^{2+}}{\mathrm{O}^{2+}}\right]. \quad (8)$$

The ionic abundances of O^+ and O^{2+} in the above equation are assumed to be those derived from the forbidden line measurements. For C^{2+} we use the results from M 1 at λ4650. The abundance derived from λ4187 is not used, since this line is much weaker than the λ4650 multiplet. The C^{4+} abundance derived from the λ4658 line is not used in deriving the total abundance, as this line may be contaminated by [Fe III]. In NGC 7009, most of the carbon should exist in the form of C^{2+} and C^{3+}, and the correction required for unobserved C^+ and C^{4+} is quite small. Equation (7) gives $icf(C) = 1.06$ for both slit PAs.

No *icf* formulation exists for the calculation of the total nitrogen abundance from the ionic abundances of N^{2+}/H and N^{3+}/H. Based on the similarity of the ionization potentials, we assume that the *icf* given by equation (7) for carbon can also be used for the case of nitrogen. As we have just mentioned, the correction is quite small, so no significant error is expected to be introduced using this approximation.

7 DISCUSSION

We found in Section 5 that for NGC 7009 the oxygen abundances derived from the recombination lines are a factor of 4.5–5 higher than those derived from the collisionally excited forbidden lines. The large discrepancy between the C^{2+} abundances derived from the recombination line C II λ4267 and from the UV collisionally excited line C III] λ1908 in NGC 7009 was first discussed by Barker (1983) in his extensive study of this object (see also Kaler 1986). In Table 13 we compare the C, N and O abundances in NGC 7009 derived from the recombination lines with those derived from the forbidden lines, and with solar photospheric abundances. Results from the PA = 45° and PA = 0° data have been averaged with equal weight. We have also included the helium abundance in Table 13.

Table 13 shows that for all three of the elements, C, N and O, studied here, the elemental abundances deduced from optical recombination lines are much higher than from the collisionally excited lines, by a remarkably constant factor of about 5. This result suggests several things. First of all, together with evidence given earlier in the paper, this strongly supports the argument that the observed large discrepancies cannot be blamed on contamination of the recombination lines by stellar continuum resonance fluorescence, since C II, N II and O II have completely different spectroscopic structures and term systems, and it is difficult to imagine how lines from these different ions could be affected *quantitatively* by the same amount by such an excitation mechanism, which depends critically on the pumping routes available. Could all the recombination coefficients used for C, N and O be underestimated by a factor of 5? This seems highly unlikely – we note that for a sample of six PNe other than NGC 7009 (Barlow et al. 1995, in preparation) the discrepancies between the abundances derived from the two types of emission lines, using the same atomic data, are much smaller, about a factor of 2 on average. Our results suggest that the same physical mechanism is responsible for the large discrepancies between the C, N as well as O abundances derived from recombination lines and from forbidden lines.

Table 13. Elemental abundances in NGC 7009 from recombination lines and forbidden lines.

	He/H	$10^4 \times$C/H	$10^4 \times$N/H	$10^4 \times$O/H
NGC 7009				
Rec.	0.109	9.24	5.12	19.2
Coll.		1.51[a]	1.25[a]	4.08
Solar[b]	0.098	3.98	1.00	8.51

[a]Barker (1983); [b]Grevesse & Anders (1989); Grevesse et al. (1990, 1991).

Among the various possibilities proposed in the past to explain the discrepancy found between the C^{2+} abundances derived from recombination lines and from collisionally excited lines, a compelling possibility is the presence of significant temperature fluctuations in PNe. The same mechanism might explain the factor of 2 lower mean oxygen abundance that has been derived from forbidden line analyses of PNe (e.g. Aller & Czyzak 1983) compared to the solar photospheric value (Grevesse & Anders 1989), as well as the systematically lower electron temperatures derived from observations of the Balmer discontinuity in nebular continuum emission, compared to the electron temperature from the [O III] forbidden line ratio. The observational evidence for the latter effect was firmly established by recent CCD spectrophotometric observations of a sample of PNe by Liu & Danziger (1993b). In the presence of temperature fluctuations, the correct abundance for a given heavy-element ion relative to hydrogen, say X^{i+}/H^+, will be that deduced from the intensity relative to Hβ of a recombination line emitted by $X^{(i-1)+}$, but will be underestimated if derived from the intensity relative to Hβ of a forbidden line emitted by X^{i+} using electron temperatures derived from forbidden line ratios. If the amplitude of the temperature fluctuations is relatively small, we can characterize the thermal structure of the nebula by a mean temperature T_0 and a temperature fluctuation parameter t^2 defined by Peimbert (1967), which can be derived by comparing two different thermometers, say the [O III] forbidden line ratio and the ratio of the nebular continuum Balmer discontinuity to Hβ. For NGC 7009, values of T_0 and t^2 thus derived have been given in Table 2, and are $T_0 = 8760$ K and $t^2 = 0.042$, averaged over the two slit positions. For $t^2 = 0.042$, the C, N and O abundances derived from the collisionally excited lines (Table 13) will increase by a factor of 1.75 after the effects of temperature fluctuations have been accounted for, which still fails by a factor of 2–3 to reconcile the abundances derived from recombination lines and collisionally excited lines. It seems that electron temperature fluctuations alone, as measured by comparing the temperatures deduced from the Balmer discontinuity and [O III] forbidden lines, cannot explain the large discrepancies between the C, N and O abundances derived from these two different types of line. Indeed, to reconcile the abundances from the two kinds of lines as listed in Table 13, t^2 values as large as 0.086, 0.072 and 0.098 are required for C, N and O, respectively.

The physical origin of the large temperature fluctuations implied by a comparison of the nebular continuum Balmer

discontinuity temperatures and the forbidden line temperatures is still not understood. It could be due to significant energy input from physical processes other than photoionization, e.g. shock waves, or be due to the presence of large-amplitude chemical composition inhomogeneities within the nebulae. Evidence in favour of these interpretations has been discussed by Peimbert (1992) and by Liu & Danziger (1993b).

Although incorporation of the effects of temperature fluctuations appears to fail to explain the large discrepancies between the C, N and O abundances deduced from recombination and collisionally excited lines, the simple treatment of temperature fluctuations outlined above is valid only if the temperature fluctuations occur ubiquitously within the nebula on scales small enough to be treated linearly. This may not be true. For example, in the presence of shock waves, there might be a thin shocked layer that has a very high temperature. Although the total radiative output from this shocked region may be negligible, it may make a significant contribution to the observed flux of [O III] λ4363, giving an unrealistically high [O III] forbidden line temperature. Indeed, if we recalculate the ionic abundances of C^{2+}/H^+, N^{2+}/H^+ and O^{2+}/H^+ from the collisionally excited lines C III] λ1908, N III] λ1750 and [O III] λ5007 with no temperature fluctuations, but using the electron temperatures deduced from the ratio of the nebular continuum Balmer discontinuity and Hβ, instead of those from the [O III] forbidden line ratio, the resultant abundances would increase by factors of 6.5, 8.2 and 2.4, respectively. Since most of the CNO atoms in NGC 7009 exist in the form of C^{2+}, N^{2+} and O^{2+}, the abundances of these three elements relative to hydrogen would also increase by similar amounts, giving C and N abundances from collisionally excited lines comparable to those from recombination lines, although still failing by a factor of 2 for oxygen. The idea of shock waves is certainly not new in planetary nebula studies. For example, interacting wind models have been widely used to explain the observed morphological types of PNe (Kwok, Purton & Fitzgerald 1978; a recent review is given by Balick 1993). The presence of shock waves is a natural result of interacting winds. Unfortunately, little work has so far been done on the possible effects of shock waves on the nebular emission-line spectrum. It would be very interesting to obtain high spectral resolution images of the [O III] λ4363 line and to look for extended wings in the profile of this line.

The C, N and O abundances derived from recombination lines in NGC 7009 are higher than the corresponding solar values by factors of 2.3, 5.1 and 2.3, respectively. On the other hand, the He abundance is not significantly different from the solar value. While it is well known that C and N can be significantly enriched in PNe by several dredge-up processes (e.g. Iben & Renzini 1983), the observed He and CNO abundance pattern in NGC 7009 does not fit into the proposed chemical evolution scenarios for progenitor stars of PNe. For example, the carbon abundance can only be enriched by the third dredge-up, taking place along the asymptotic giant branch (AGB) following thermal relaxation oscillations (helium shell flashes). After the third dredge-up, the helium abundance should also be enhanced, in contrast to what is observed for NGC 7009. In addition, there is no currently known process that could enhance the oxygen abundance in PNe by a factor of 2 or more. One possibility is that NGC 7009 is a peculiar PN which formed in a region where the metal abundance of the ISM was much higher than the average. Whether or not NGC 7009 is peculiar in this respect among the Galactic PNe can be established by extending the analysis reported in this work to additional objects. A first step towards this goal is reported in a companion paper (Barlow et al. 1995, in preparation).

8 SUMMARY

Excellent agreement is found between the relative intensities of the rich O II recombination line spectrum of NGC 7009 and intermediate coupling calculations for their radiative recombination coefficients. This greatly strengthens our confidence in the reliability of current recombination theory for non-hydrogenic ions. The close agreement between the abundances deduced from lines from different multiplets and electron configurations supports the interpretation of the observed lines as due to recombination. Contamination from other excitation mechanisms, if any, should be negligible. The C, N and O abundances derived for NGC 7009 from recombination lines are all found to be higher by a factor of 5 than the corresponding values deduced from collisionally excited lines, indicating that the discrepancy between the abundances derived from these two different types of emission lines, previously known to exist for C^{2+}, is a common phenomenon and is probably caused by the same physical process. The nature of this process is still not known; careful high-S/N ratio mapping at high spatial resolution of the electron temperature, electron density and elemental abundances across the surface of NGC 7009 may provide clues to the solution. At the moment, instead of simply blaming the discrepancy on inaccuracies in the effective recombination coefficients or on contamination of the recombination lines by processes such as stellar continuum resonance fluorescence, possible systematic effects in the classic plasma analysis procedure based entirely on forbidden-line measurements should also be investigated, especially the validity of electron temperature derived from the [O III] nebular to auroral line ratio.

The abnormally high C, N and O abundances found in NGC 7009 from our analysis of the optical recombination lines, if real, may indicate that NGC 7009 formed in a region where the metal abundance was much higher than the current average Galactic value.

REFERENCES

Aller L. H., Czyzak S. J., 1979, Ap&SS, 62, 397
Aller L. H., Czyzak S. J., 1983, ApJS, 51, 211
Aller L. H., Kaler J. B., 1964, ApJ, 139, 1074
Aller L. H., Keyes C. D., 1987, ApJS, 65, 392
Balick B., 1993, in Weinberger R., Acker A., eds, Proc. IAU Symp. 155, Planetary Nebulae. Kluwer, Dordrecht, p. 131
Barker T., 1983, ApJ, 267, 630
Barker T., 1991, ApJ, 371, 217
Barlow M. J., Storey P. J., 1993, in Weinberger R., Acker A., eds, Proc. IAU Symp. 155, Planetary Nebulae. Kluwer, Dordrecht, p. 92
Clegg R. E. S., 1987a, in Torres-Peimbert S., ed., Proc. IAU Symp. 131, Planetary Nebulae. Kluwer, Dordrecht, p. 139
Clegg R. E. S., 1987b, MNRAS, 229, L31

Clegg R. E. S., Harrington J. P., Barlow M. J., Walsh J. R., 1987, ApJ, 314, 551
Cunto W., Mendoza C., Ochsenbein F., Zeippen C. J., 1993, A&A, 275, L5
Eissner W., Jones M., Nussbaumer H., 1974, Comput. Phys. Commun., 15, 23
Escalante V., Victor G. A., 1990, ApJS, 73, 513
French H. B., 1983, ApJ, 273, 214
Grandi S. A., 1976, ApJ, 206, 658
Grevesse N., Anders E., 1989, in Waddington, C. J., ed., AIP Conf. Proc. 183, Cosmic Abundances of Matter. Am. Inst. Phys., New York, p. 1
Grevesse N., Lambert D. L., Sauval A. J., van Dishoeck E. F., Farmer C. B., Norton R. H., 1990, A&A, 232, 225
Grevesse N., Lambert D. L., Sauval A. J., van Dishoeck E. F., Farmer C. B., Norton R. H., 1991, A&A, 242, 488
Hamuy M., Walker A. R., Suntzeff N. B., Gigoux P., Heathcote S. R., Phillips M. M., 1992, PASP, 104, 533
Howarth I. D., Murray J., 1988, SERC Starlink User Note No. 50
Hummer D. G., Storey P. J., 1987, MNRAS, 224, 801
Iben I., Jr, Renzini A., 1983, ARA&A, 21, 271
Kaler J. B., 1976, ApJS, 31, 517
Kaler J. B., 1986, ApJ, 308, 322
Kaler J. B., Aller L. H., 1969, ApJ, 157, 1231
Kingsburgh R. L., Barlow M. J., 1995, MNRAS, in press
Kwok S., Purton C. R., Fitzgerald M. P., 1978, ApJ, 219, L125
Liu X. W., Danziger I. J., 1993a, MNRAS, 261, 465
Liu X. W., Danziger I. J., 1993b, MNRAS, 263, 256
Monk D. J., Barlow M. J., Clegg R. E. S., 1990, MNRAS, 242, 457
Moore C. E., 1972, A Multiplet Table of Astrophysical Interest. National Bureau of Standards, No. 40
Nikitin A. A., Kholtygin A. F., Sapar A., Feklistova T., 1993, Baltic Astron., 1
Nikitin A. A., Kholtygin A. F., Sapar A., Feklistova T., 1987, in Torres-Peimbert S., ed., Proc. IAU Symp. 131, Planetary Nebulae. Kluwer, Dordrecht, p. 218
Nussbaumer H., Storey P. J., 1978, A&A, 64, 13
Nussbaumer H., Storey P. J., 1984, A&AS, 56, 293
Oke J. B., 1974, ApJS, 27, 21
Peimbert M., 1967, ApJ, 150, 825
Peimbert M., 1971, Bol. Obs. Tonantzintla y Tacubaya, 6, 29
Peimbert M., 1992, in Edmunds M. G., Terlevich R. J., eds, Elements and the Cosmos. Cambridge Univ. Press, Cambridge, p. 196
Peimbert M., Sarmiento A., Fierro J., 1991, PASP, 103, 815
Peimbert M., Storey P. J., Torres-Peimbert S., 1993, ApJ, 414, 626
Péquignot D., Petitjean P., Boisson C., 1991, A&A, 251, 680
Seaton M. J., 1979, MNRAS, 187, L73
Stone R. P. S., Baldwin J. A., 1983, MNRAS, 204, 347
Storey P. J., 1994, A&A, 282, 999
Wenåker I., 1990, Phys. Scr., 42, 667